J Adv Ceram

Research Article

First-principles insights into solid solution mechanisms of doped $Gd_2Zr_2O_7$ and guides to develop novel thermal barrier coating materials

Kun Wang[1,2,3], Lei Guo[1,2,3,✉], Xiaohu Yuan[4], Wei Wang[4], Xiufang Gong[4,✉]

Cite this article: Wang K, Guo L, YuanX, et al. *J Adv Ceram* 2026, **15**(6): 9221295. https://doi.org/10.26599/JAC.2026.9221295

ABSTRACT: $Gd_2Zr_2O_7$ (GZO)-based compounds are currently one of the most promising materials for thermal barrier coatings (TBCs), in which some dopants are introduced. The dopants induce changes in the GZO lattice and improve the properties; however, the underlying mechanisms related to the solid solution modes of the dopant remain insufficiently understood. In this study, first-principles calculations were employed to investigate the solid solution mechanism of Yb and Sc codoping in GZO. The results showed that both substitutional and interstitial doping coexist in the GZO lattice. At a Yb doping content of 12.5 at%, a substitutional solid solution formed in the GZO lattice, and with further introduction of Sc into the lattice, the Sc atom occupied interstitial sites at concentrations below 5.88 at%. The calculation results indicate that 11.76 at% Yb and 5.88 at% Sc codoped GZO (GYbSc) exhibited the lowest thermal conductivity, the highest coefficient of thermal expansion (CTE), and relatively high toughness. Experimental results demonstrated that GYbSc exhibits high toughness (2.09 $MPa{\cdot}m^{1/2}$). At 1200 °C, the coefficient of thermal expansion of GYbSc increased by 5% compared with that of GZO, and its thermal conductivity decreased by 37%, with values of 11.059×10^{-6} and 0.935 $W{\cdot}m^{-1}{\cdot}K^{-1}$, respectively. GYbSc also displayed outstanding CaO–MgO–Al_2O_3–SiO_2 (CMAS) corrosion resistance. This work not only explores a promising TBC material but also provides a new perspective for clarifying the mechanisms for the improved properties of doped compounds and developing novel TBC materials.

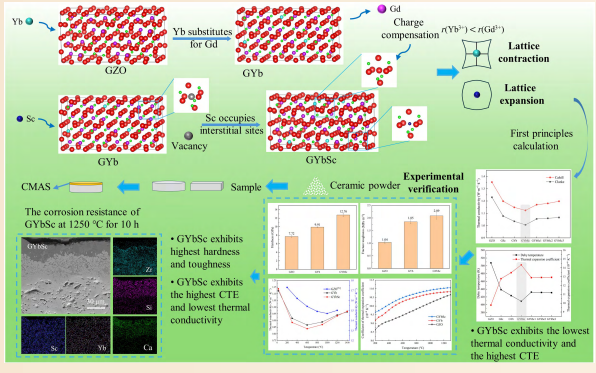

KEYWORDS: thermal barrier coating; first-principles calculation; solid solution mechanism; Yb–Sc codoping; thermophysical properties; CaO–MgO–Al_2O_3–SiO_2 corrosion

1 Introduction

Thermal barrier coating (TBC) is widely used in the turbine blades of aeroengines to improve the service life of turbine blades, the thrust weight ratio, and the efficiency of engines [1,2]. The widely used TBC material is 6–8 wt% Y_2O_3-stabilized ZrO_2 (YSZ), which has low thermal conductivity, high coefficient of thermal expansion, and high fracture toughness [3]. However, prolonged exposure of YSZ TBCs to temperatures above 1200 °C induces a phase transformation from the tetragonal phase to the monoclinic phase, which is associated with a large volume expansion [4]. Additionally, YSZ TBCs are very susceptible to corrosion by environmental deposits composed of CaO–MgO–Al_2O_3–SiO_2 (CMAS), causing premature failure of the coating [5,6]. Compared with YSZ, $RE_2Zr_2O_7$ (RE: rare earth elements) has excellent high-temperature phase stability, reduced thermal conductivity, and superior resistance to CMAS corrosion [7]. Among them, $Gd_2Zr_2O_7$ (GZO) performs more prominently and is one of the most highly regarded candidates for TBCs.

Existing research indicates that the properties of GZO can be further improved by the doping strategy. Shen *et al.* [8] doped GZO with Er_2O_3, reducing the thermal conductivity at 800 °C to 1.02 $W{\cdot}m^{-1}{\cdot}K^{-1}$. Lee *et al.* [9] used Y_2O_3 to modify GZO, raising the coefficient of thermal expansion close to that of YSZ and increasing the hardness to 10 GPa. Yan *et al.* [10] indicated that Ti and Ce doping effectively improved the thermophysical properties of the material. Researchers attribute the enhanced mechanical and thermophysical properties of doped GZO to the change in the crystal structure, such as lattice distortion, ordering degree change, atomic mass difference, and ionic radius difference [8–10]. It is

[1] School of Materials Science and Engineering, Tianjin University, Tianjin 300072, China. [2] State Key Laboratory of Precious Metal Functional Materials, Tianjin 300072, China. [3] Tianjin Key Laboratory of Advanced Joining Technology, Tianjin 300072, China. [4] State Key Laboratory of Clean and Efficient Turbomachinery Power Equipment, Deyang 618000, China.

✉ Corresponding authors. E-mail: L. Guo, glei028@tju.edu.cn; X. Gong, gongxiufang@dongfang.com

Received: January 9, 2026; Revised: March 5, 2026; Accepted: April 9, 2026

obvious that the crystal structure change is caused by the introduction of dopants into the GZO lattice, and the degree of change is closely related to the solid solution mechanisms of the dopants. There are two solid solution modes for the doped atoms in the GZO lattice: substitutional doping and interstitial doping. Although both can cause crystal structure changes, their effects on the mechanical and thermophysical properties of the material are different. In most existing studies, rare earth dopants are implicitly assumed to form substitutional solid solutions by substituting for Gd. Nevertheless, as the ionic radius of rare earth elements decreases, the propensity of these ions to occupy interstitial sites within the lattice increases, which may fundamentally alter the properties of doped GZO.

Traditional experimental approaches primarily rely on repetitive trial-and-error and testing to indirectly infer the solid solution mechanism of dopants. Such an approach is not only relatively inefficient but also involves considerable research costs. Compared with traditional experiments, first-principles calculations can save a great deal of time and experimental costs. First-principles calculations based on density functional theory (DFT) can reveal the electronic structure, lattice dynamics, and thermal transport mechanism of materials at the atomic scale and are particularly suitable for the rapid screening and mechanism analysis of multicomponent doped systems [11,12]. In recent years, first-principles calculations have been widely applied in fields such as alloys, semiconductors, and optoelectronic devices. Among them, the solid solution mechanism of doped elements is analyzed by defect formation energy calculations, and the influence of doping on alloy properties, conductivity types, and other aspects is easy to clarify [13,14]. Hence, to directly describe and reveal the solid solution mechanism of dopants, first-principles calculations should be strongly encouraged in the TBC field, by which novel TBC material design can be accelerated.

Studies have shown that the solid solution mechanism of Yb-doped GZO follows a substitutional doping process, where Yb replaces Gd in the GZO lattice to form Yb-doped GZO. The ionic radius of Yb^{3+} (0.985 Å) is smaller than that of Gd^{3+} (1.053 Å), and the relative atomic mass of Yb (173.05) is greater than that of Gd (157.25). When Yb is doped into GZO, the resulting mass and strain fluctuations intensify phonon scattering, shortening the phonon mean free path and significantly reducing the thermal conductivity of the material [15–17]. In our previous study, we successfully clarified the solid solution mechanisms of Sc in the GZO lattice using first-principles calculations [18]. The results revealed that there are two solid solution modes in the Sc-doped GZO lattice: interstitial doping at a low doping content and substitutional doping as the doping content increases. This special solid solution mode is due to the smaller radius of Sc^{3+} (0.870 Å) than that of the lanthanide rare earth elements. Furthermore, the mechanical and thermophysical properties of Sc-doped GZO were investigated by both first-principles calculations and experimental measurements, demonstrating that Sc doping into GZO can not only reduce the thermal conductivity but also effectively enhance the fracture toughness and CMAS resistance [18,19]. After clarifying the solid solution mode of Sc, the underlying mechanism for the improved properties of Sc-doped GZO has been well revealed.

In conclusion, the smaller ionic radii of Yb^{3+} and Sc^{3+} provide more possibilities for the doping of rare earth elements. In this study, we designed a promising TBC material by in-depth analysis of the solid solution mechanisms of Yb and Sc in the GZO lattice. In the Yb–Sc codoped GZO lattice, the coexistence of substitutional and interstitial doping was demonstrated by first-principles calculations, which effectively reduced the thermal conductivity while simultaneously enhancing the fracture toughness. Based on the calculation results, the optimal compositions were selected for experimental preparation, and their mechanical properties, phase stability, thermophysical properties, and resistance to CMAS corrosion were evaluated. This study profoundly demonstrates that by using simulation calculations to reveal the underlying mechanism and abandoning the traditional trial-and-error approach, novel TBC materials could be explored more accurately and rapidly.

2 Calculation details and experimental procedure

2.1 Calculation details

The $Gd_2Zr_2O_7$ and $(Gd_{1-x-y}Sc_xYb_y)_2Zr_2O_7$ series models were constructed using Material Studio software, and all density functional theory (DFT) calculations were conducted using the Vienna *ab initio* simulation package (VASP) [20]. The calculations used the projector augmented-wave (PAW) method to describe the interaction between electrons and ions, and the generalized gradient approximation (GGA) was used to treat the electronic exchange–correlation potential [21,22]. The cutoff energy was set to 500 eV, and the k-point mesh used the Gamma-point scheme for the Brillouin zone. The k-point for the supercell was set to 1×3×3. The f-shell electrons of rare earth elements give rise to strong electronic Coulomb interactions. Since the f-shell electrons have little influence on the calculation results of the mechanical and thermophysical properties of the structure, the f-shell electrons of rare earth elements are treated as core electrons during the calculation process in this study. During structural optimization, a coarse optimization was first performed. The convergence criterion for the electronic step was set to 1×10^{-4} eV, and that for the ionic step was set to 0.05 eV. Subsequently, a fine optimization was carried out, tightening the convergence criterion of the electronic step to 1×10^{-6} eV and that of the ion step to 0.01 eV to ensure the accuracy and reliability of the calculation results.

To systematically study the influence of different doping modes on material properties, a 2×1×1 $Gd_2Zr_2O_7$ (GZO) supercell was used for simulation in this study. Based on this crystal cell, three doping models were constructed: 12.5 at% Yb_2O_3-doped GZO, 5.88 at% Sc_2O_3-doped GZO, and a codoped GZO system with Sc_2O_3 and Yb_2O_3. To investigate the solid solution mechanism of Yb and Sc during the doping process, the defect formation energy (E_f) for different models was calculated using Eq. (1) [18,23]:

$$E_f = E_{tot}[\text{defect}] - E_{tot}[\text{perfect}] - \sum_i n_i\mu_i \quad (1)$$

where E_{tot}[defect] represents the total energy of the defective cell after doping; E_{tot}[perfect] is the total energy of the GZO unit cell or supercell; μ_i represents the chemical potential of the i atom; n_i is the number of i atoms involved in the defect. During the doping process, if atoms are introduced into the unit cell, $n_i > 0$; if atoms are removed from the unit cell, $n_i < 0$. A single atom is placed in an empty unit cell with no symmetry constraints, and the structure is optimized. When the unit cell is in the lowest energy state, the corresponding energy is taken as μ_i of the atom. This method is used to calculate the μ_i of Gd, Yb, Sc, and O.

The elastic constants of the selected models were calculated. GZO belongs to the cubic crystal system and has three independent elastic constants: C_{11}, C_{12}, and C_{44}. If the elastic constants of the crystal structure satisfy the mechanical stability

criteria, as given by Eq. (2), the structure can be considered mechanically stable [24]:

$$\begin{cases} C_{11} > 0 \\ C_{44} > 0 \\ C_{11} > |C_{12}| \\ (C_{11} + 2C_{12}) > 0 \end{cases} \tag{2}$$

Based on the calculated elastic constant, the bulk modulus (B) and shear modulus (G) of cubic crystal materials can be further derived. Using the Voigt and Reuss models, the B and G of these crystal system structures can be calculated by Eqs. (3)–(5) [25,26]:

$$B_V = B_R = (C_{11} + 2C_{12})/3 \tag{3}$$

$$G_V = (C_{11} - C_{12} + 3C_{44})/5 \tag{4}$$

$$G_R = 5(C_{11} - C_{12})C_{44}/[4C_{44} + 3(C_{11} - C_{12})] \tag{5}$$

Based on the theoretical frameworks proposed by Voigt and Reuss, Hill [27] introduced the Voigt–Reuss–Hill (VRH) averaging scheme. This approach estimates the B and G of the material as the average of the values obtained from the Voigt and Reuss approximations, which can be expressed as Eqs. (6) and (7) [27,28]:

$$B_{VRH} = \frac{B_V + B_R}{2} \tag{6}$$

$$G_{VRH} = \frac{G_V + G_R}{2} \tag{7}$$

Based on the B and G estimated using the VRH approach, the Young's modulus (E) and Poisson's ratio (σ) of the material can be further calculated using Eqs. (8) and (9) [29]:

$$E = \frac{9BG}{3B + G} \tag{8}$$

$$\sigma = \frac{3B - 2G}{2(3B + G)} \tag{9}$$

Based on the calculated elastic modulus, the longitudinal acoustic velocity (v_l), transverse acoustic velocity (v_t), and average acoustic velocity (v_m) of the material can be calculated using Eqs. (10)–(12) [30,31]:

$$v_l = \sqrt{\left(B + \frac{4}{3}G\right)/\rho} \tag{10}$$

$$v_t = \sqrt{G/\rho} \tag{11}$$

$$v_m = \left[\frac{1}{3}\left(\frac{2}{v_t^3} + \frac{1}{v_l^3}\right)\right]^{-\frac{1}{3}} \tag{12}$$

Based on the calculated sound velocities, the Debye temperature (Θ) of the material can be further determined. The Debye temperature can be calculated using Eq. (13) [30,31]:

$$\Theta = \frac{h}{k_B}\left[\frac{3n}{4\pi}\left(\frac{N_A\rho}{M}\right)\right]^{\frac{1}{3}} v_m \tag{13}$$

where h is Planck's constant; k_B is Boltzmann's constant; n represents the number of atoms in the unit cell; N_A is Avogadro's constant; ρ is the density of the unit cell; M is the molar mass of the unit cell.

Combining the Gruneisen equation with the Debye heat capacity model, Wang *et al.* [32] proposed an effective calculation model for the coefficient of thermal expansion (CTE) at high temperatures, which is expressed as Eq. (14):

$$\alpha_\infty = \frac{3nN_Ak_B}{2BV}\frac{1+\sigma}{2-3\sigma} \tag{14}$$

where σ represents the Poisson's ratio of the crystal; B is the bulk modulus of the unit cell; V is the volume of the unit cell.

The minimum thermal conductivity is the lower limit of thermal conductivity at high temperatures, reflecting the heat transfer characteristics of materials at high temperatures. Based on the above calculation results, this study uses the Clarke and Cahill models to calculate the minimum thermal conductivity of the material, which are expressed as Eqs. (15) and (16) [33–35]:

$$K_{min}^{Clarke} = 0.87k_B\left(\frac{M}{n\rho N_A}\right)^{-\frac{2}{3}}\sqrt{\frac{E}{\rho}} \tag{15}$$

$$K_{min}^{Cahill} = \frac{k_B}{2.48}\left(\frac{n}{V}\right)^{\frac{2}{3}}(v_l + 2v_t) \tag{16}$$

2.2 Experimental procedure

GZO, Yb-doped GZO (GYb), and Sc–Yb-codoped GZO (GYbSc) powders were prepared by the chemical coprecipitation method [36]. Taking GYbSc as an example, Gd_2O_3, Yb_2O_3, Sc_2O_3, and $ZrOCl_2{\cdot}8H_2O$ were weighed at a molar ratio of 14 : 2 : 1 : 34. Sc_2O_3, Yb_2O_3, and Gd_2O_3 were dissolved in concentrated nitric acid (65%, Jiangtian Chemical Reagents Co., Ltd., Tianjin, China) to form $Sc(NO_3)_3$, $Yb(NO_3)_3$, and $Gd(NO_3)_3$, while $ZrOCl_2{\cdot}8H_2O$ was dissolved in deionized water. The four solutions were mixed thoroughly and then slowly dropped into excess ammonium hydroxide under simultaneous ultrasonic treatment and mechanical stirring to ensure homogeneous precipitation. At the end of the reaction, the products were separated by centrifugation and washed with deionized water and ethanol until the pH reached 7.

The molar ratio of Gd_2O_3 and $ZrOCl_2{\cdot}8H_2O$ was fixed at 1 : 2 for the preparation of GZO. For the synthesis of GYb, the molar ratio of Gd_2O_3, Yb_2O_3, and $ZrOCl_2{\cdot}8H_2O$ was set to 7 : 1 : 16. The rest of the preparation processes were the same as those described above for preparing GYbSc. After centrifugation, the products were dried at 120 °C for 10 h and then calcined at 900 °C for 5 h for crystallization. The crystallized powder was ground and sieved and then pressed into pellets using a mold with a diameter of 15 mm. The pellet material was sintered at 1600 °C for 10 h to obtain the pellets used in the experiment.

The hardness and fracture toughness of the block material were measured by the indentation method using a Vickers hardness tester. The test load was 0.5 kg, and the loading time was 15 s. The fracture toughness of the material was calculated using the indentation method, as given by Eq. (17) [37]:

$$K_{IC} = 0.16H_Va^2c^{-\frac{3}{2}} \tag{17}$$

where H_V represents the Vickers hardness of the sample; a is the half-length of the diagonal of the indentation; c is the length from the midpoint of the indentation to the tip of the crack.

The CTE of the material was tested using a high-temperature thermal expansion meter (DIL 402C). During the test, the sample

was heated from room temperature to 1300 °C at a heating rate of 10 °C·min^{-1}. The thermal diffusivity of the material was tested using an ultrahigh-temperature laser thermal conductivity meter (DLF2800), and the specific heat capacity of the material from room temperature to 1400 °C was tested using a differential scanning calorimeter (DSC 8000) and a high-temperature calorimeter (MHTC96).

The phases of the thermal barrier coating materials and the phases of these materials after corrosion by CMAS were characterized using an X-ray diffractometer (XRD; Bruker D8 Advanced, Germany). The scanning range was from 10° to 85° with a scanning rate of 0.2° s^{-1}, and the current and voltage were 40 mA and 40 kV, respectively. Cross-sectional microstructures of the samples were observed, and compositional analysis was performed using a scanning electron microscope (SEM; Nanosem 430, FEI, USA) equipped with energy-dispersive X-ray spectroscopy (EDS; IE 350, Penta FET X-3, UK) operated at an acceleration voltage of 15 kV.

The composition of CMAS was determined through EDS analysis of the environmental deposits on turbine blades, with its components presented in Table 1. The actual engine deposits may have slight fluctuations in impurities due to differences in flight environment, region, and operating conditions, but their main chemical composition is consistent with the CMAS system in this study. Therefore, this CMAS component can well reflect the erosion behavior of the deposits on the thermal barrier coating under actual service conditions and can provide a reliable simulation basis for related failure mechanism research. The analytically pure oxide powders of CaO, MgO, Al_2O_3, SiO_2, NiO, TiO_2, Na_2SO_4, and $CaSO_4$ were sourced from Tianjin Jiangtian Chemical Technology Co., Ltd., and analytically pure Fe_2O_3 was sourced from Shanghai Macklin Biochemical Technology Co., Ltd. They were weighed according to the mass ratio and mixed with ethanol. The obtained suspension was placed in a ball mill jar and ground at a speed of 400 r·min^{-1} for 8 h. The slurry obtained by ball milling was dried at 120 °C in a drying oven for 10 h. Subsequently, the dried powder was heated in a box furnace, with the temperature raised to 1550 °C and held for 1 h. The molten CMAS was poured into a beaker filled with deionized water to obtain CMAS glass. Finally, the obtained glass was ground and sieved to obtain the CMAS powder for corrosion tests.

In the corrosion test, CMAS was coated on the surface of the block material at a coating density of 15 mg·cm^{-2}. The samples were placed in a box furnace at 1250 °C for heat treatment for 10 and 15 h and then cooled to room temperature inside the furnace. Based on the samples after 15 h of heat treatment, CMAS powder was reapplied at a coating density of 10 mg·cm^{-2}, and the samples were again placed in a box furnace at 1250 °C for 10 min, 5 h, and 10 h of heat treatment.

3 Results and discussion

3.1 Lattice models of doped GZO crystals and solid solution mechanism of doping atoms in lattice

The optimized structures of the 2×1×1 GZO model are shown in Fig. 1(a). When Sc is introduced into the GZO lattice, Sc tends to occupy interstitial sites when its doping content is below 11.11 at% [19]. The model of 5.88 at% Sc-doped GZO (GSc) is shown in Fig. 1(b). Previous studies have demonstrated that doping GZO with Yb can significantly reduce its thermal conductivity [11]. However, the underlying solid solution mechanism of Yb within the GZO lattice has not been fully elucidated. The defect formation energy is an important parameter for evaluating the formation possibility of a point defect and has been widely used by many scholars to clarify the solid solution mechanism of dopant atoms [23]. A lower defect formation energy indicates that the corresponding defect is more likely to form, implying that doping at that site is more favorable and that a relatively more stable structure can be obtained. By calculating the defect formation energy of Yb-doped GZO and Yb–Sc-codoped GZO, we studied the solid solution mechanism of Yb and Sc in the GZO lattice.

Figure S1 in the Electronic Supplementary Material (ESM) shows the 2 × 1 × 1 Yb-doped GZO models, where there are four Yb atoms introduced into the GZO lattice. It has been reported that the 32e (0.25, 0.25, 0.25) site is the most stable interstitial position in the GZO lattice [23]. Therefore, this position was selected as the interstitial site. In Fig. S1(a) in the ESM, four Yb atoms all substitute for Gd, and the formula could be written as GZO–$Yb_{4\text{-sub}}$. In Figs. S1(b)–S1(e) in the ESM, three Yb atoms substitute for Gd atoms and one Yb atom occupies an interstitial site; two Yb atoms substitute for Gd atoms and two Yb atoms occupy interstitial sites; one Yb atom substitutes for Gd and three Yb atoms occupy interstitial sites; and four Yb atoms all occupy interstitial sites. The formulas of these models in Figs. S1(b)–S1(e) in the ESM are written as GZO–$Yb_{1\text{-in+3-sub}}$, GZO–$Yb_{2\text{-in+2-sub}}$, GZO–$Yb_{3\text{-in+1-sub}}$, and GZO–$Yb_{4\text{-in}}$, respectively, and their defect formation energies are calculated and listed in Table 2. By comparison, GZO–$Yb_{4\text{-sub}}$ has the lowest defect formation energy, revealing that when doping four Yb atoms into the GZO lattice, the Yb solid solution mechanism is that all Yb atoms substitute for Gd. The optimized model of GZO–$Yb_{4\text{-sub}}$ (12.5 at% Yb-doped GZO, GYb) is shown in Fig. 1(c).

It has been reported that Sc doping into GZO can improve the thermoproperties [14,19]. Hence, to further improve the properties of GYb, we introduced Sc into GYb to form composition A, i.e., doping two Sc into the model in Fig. 1(b). There are three possible lattice models for composition A: two Sc atoms all occupy interstitial sites (Fig. S2(a) in the ESM, GZO–$Yb_{4\text{-sub}}$–$Sc_{2\text{-in}}$), one Sc atom occupies an interstitial site and one substitutes for Gd (Fig. S2(b) in the ESM, GZO–$Yb_{4\text{-sub}}$–$Sc_{1\text{-in+1-sub}}$), and two Sc atoms all substitute for Gd (Fig. S2(c) in the ESM, GZO–$Yb_{4\text{-sub}}$–$Sc_{2\text{-sub}}$). The corresponding defect formation energies are calculated to be 12.34, 13.11, and 15.62 eV, respectively, with that of GZO–$Yb_{4\text{-sub}}$–$Sc_{2\text{-in}}$ exhibiting the lowest value in composition A. Therefore, the solid solution mechanism of composition A is that two Sc atoms occupy interstitial sites (GZO–$Yb_{4\text{-sub}}$–$Sc_{2\text{-in}}$, GYbSc4), and the optimized structure is shown in Fig. 1(d). In this structure, the interstitial sites occupied by Sc are 32e (0.25, 0.25, 0.25). The crystal structure of pyrochlore has a typical face-centered cubic symmetry. Its lattice is composed of BO_6 octahedra connected at common angles, and the 32e sites are the pre-existing interstitial positions in this structure [38]. Their geometric dimensions have a natural compatibility with the

Table 1 Components of CMAS

Content	CaO	MgO	Al_2O_3	SiO_2	Fe_2O_3	NiO	TiO_2	Na_2SO_4	$CaSO_4$
(mol%)	28.50	10.52	16.77	30.05	5.32	5.82	2.80	0.15	0.17
(wt%)	22.58	5.99	24.01	25.50	11.99	6.14	3.16	0.29	0.33

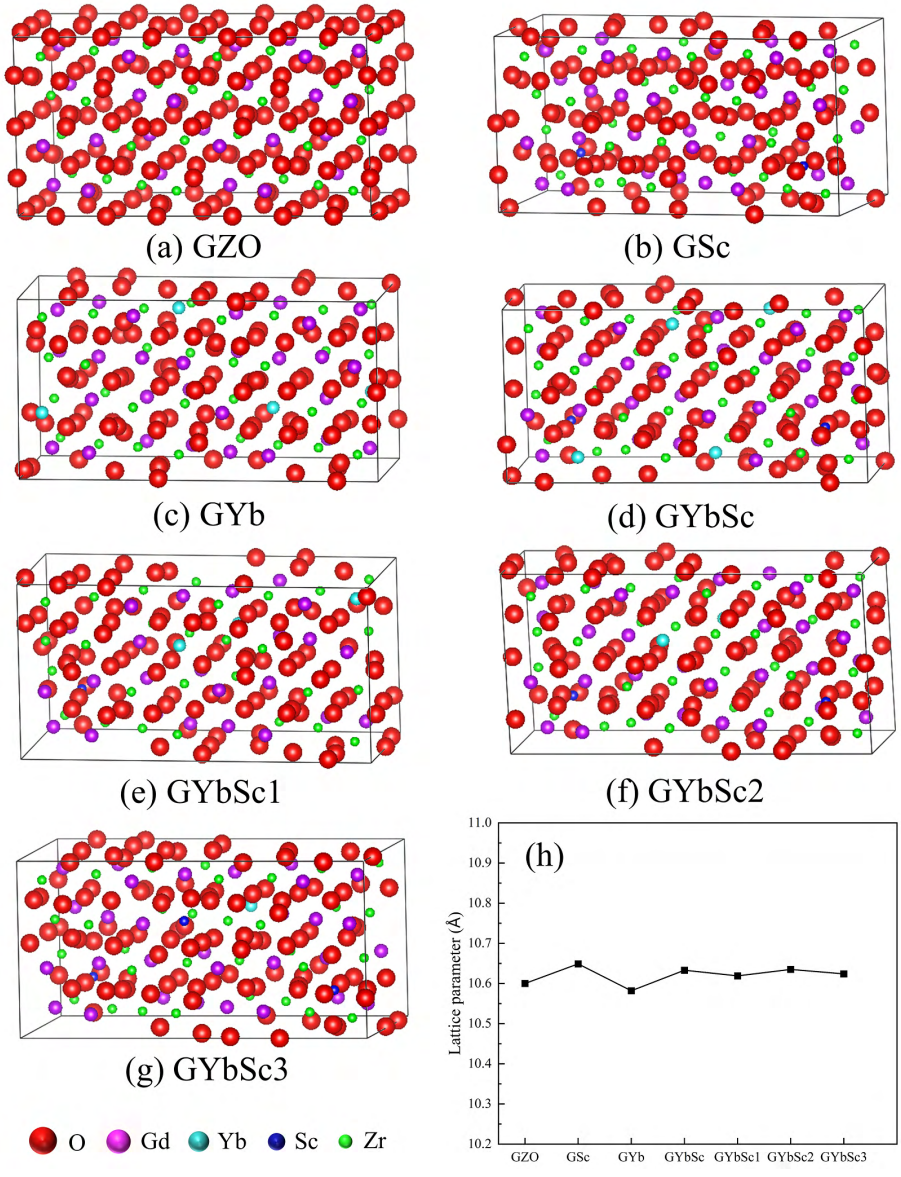

Fig. 1 (a) GZO model, (b) GSc model, (c) GYb model, (d–g) Yb and Sc codoped GZO models, and (h) variations in their lattice constants.

sizes of the rare earth cations. On the other hand, after the cations occupy this site, the spatial distribution of the surrounding coordination atoms is uniform, which can minimize the lattice stress.

Meanwhile, three compositions were designed, which have similar total contents of Yb and Sc (~12.5 at%), as summarized in Table 2. The 2×1×1 models of composition B are shown in Fig. S2 in the ESM, which contain one Sc atom and three Yb atoms. Research on Yb-doped GZO indicates that Yb substitutes for Gd. Since Sc has a small size, it has the possibility of occupying the interstitial site in addition to substituting for Gd. Figures S2(d) and S2(e) in the ESM show two possible lattice models of composition B, i.e., the Sc atom occupies an interstitial site (Fig. S2(d) in the ESM, GZO–$Yb_{3\text{-sub}}$–$Sc_{1\text{-in}}$), and it substitutes for Gd (Fig. S2(e) in the ESM, GZO–$Yb_{3\text{-sub}}$–$Sc_{1\text{-sub}}$). The defect formation energies of GZO–$Yb_{3\text{-sub}}$–$Sc_{1\text{-in}}$ and GZO–$Yb_{3\text{-sub}}$–$Sc_{1\text{-sub}}$ were calculated to be 4.52 and 16.82 eV, respectively, with GZO–$Yb_{3\text{-sub}}$–$Sc_{1\text{-in}}$ exhibiting a lower value in composition B. Therefore, the solid solution mechanism of dopants in composition B is that the Sc atom occupies an interstitial site (GZO–$Yb_{3\text{-sub}}$–$Sc_{1\text{-in}}$, GYbSc1), and the optimized structure is shown in Fig. 1(e). As shown in Fig. S2(f)–S2(h) in the ESM, composition C contains two Sc atoms and two Yb atoms, with three possible lattice models, i.e., both Sc atoms occupy interstitial sites (Fig. S2(f) in the ESM, GZO–$Yb_{2\text{-sub}}$–$Sc_{2\text{-in}}$), one Sc atom occupies an interstitial site and one substitutes for Gd (Fig. S2(g) in the ESM, GZO–$Yb_{2\text{-sub}}$–$Sc_{1\text{-in+1-sub}}$), and both Sc atoms substitute for Gd (Fig. S2(h) in the ESM, GZO–$Yb_{2\text{-sub}}$–$Sc_{2\text{-sub}}$). The defect formation energy values of these three configurations were determined to be 3.51, 14.73, and 9.63 eV, respectively. Among them, GZO–$Yb_{2\text{-sub}}$–$Sc_{2\text{-in}}$ has the lowest value in composition C. Consequently, the solid solution mechanism of the dopants in composition C is that both Sc atoms occupy interstitial sites (GZO–$Yb_{2\text{-sub}}$–$Sc_{2\text{-in}}$, GYbSc2), and its optimized structure is shown in Fig. 1(f). Similarly, the models of composition D contain three Sc atoms and one Yb atom. Defect formation energy calculations indicate that GZO–$Yb_{1\text{-sub}}$–$Sc_{2\text{-in+1-sub}}$ possesses the lowest energy in this composition. Consequently, the solid solution mechanism of the dopants in composition D is that two Sc atoms occupy interstitial sites and one substitutes for Gd (GZO–$Yb_{1\text{-sub}}$–$Sc_{2\text{-in+1-sub}}$, GYbSc3), and its optimized structure is shown in Fig. 1(g).

Table 2 Doping ratio and lattice parameters of different models

		Sc (at%)	Yb (at%)	a_0 (Å)	E_f (eV)
	GZO	0%	0%	10.600	—
	GZO–Sc (GSc)	5.88%	0%	10.649	—
	GZO–$Yb_{4\text{-sub}}$ (GYb)	0%	12.5%	10.582	8.79
	GZO–$Yb_{1\text{-in+3-sub}}$	0%	12.12%	10.617	11.54
	GZO–$Yb_{2\text{-in+2-sub}}$	0%	11.76%	10.632	16.38
	GZO–$Yb_{3\text{-in+1-sub}}$	0%	11.43%	10.651	20.37
	GZO–$Yb_{4\text{-in}}$	0%	11.11%	10.668	32.91
A	GZO–$Yb_{4\text{-sub}}$–$Sc_{2\text{-in}}$ (GYbSc)	5.88%	11.76%	10.633	12.34
	GZO–$Yb_{4\text{-sub}}$–$Sc_{1\text{-in+1-sub}}$	6.06%	12.12%	10.597	13.11
	GZO–$Yb_{4\text{-sub}}$–$Sc_{2\text{-sub}}$	6.25%	12.5%	10.589	15.62
B	GZO–$Yb_{3\text{-sub}}$–$Sc_{1\text{-in}}$ (GYbSc1)	3.03%	9.09%	10.619	4.52
	GZO–$Yb_{3\text{-sub}}$–$Sc_{1\text{-sub}}$	3.13%	9.38%	10.581	16.82
C	GZO–$Yb_{2\text{-sub}}$–$Sc_{2\text{-in}}$ (GYbSc2)	5.88%	5.88%	10.635	3.51
	GZO–$Yb_{2\text{-sub}}$–$Sc_{1\text{-in+1-sub}}$	6.06%	6.06%	10.627	14.73
	GZO–$Yb_{2\text{-sub}}$–$Sc_{2\text{-sub}}$	6.25%	6.25%	10.585	9.63
D	GZO–$Yb_{1\text{-sub}}$–$Sc_{3\text{-in}}$	8.57%	2.86%	10.625	9.75
	GZO–$Yb_{1\text{-sub}}$–$Sc_{2\text{-in+1-sub}}$ (GYbSc3)	8.82%	2.94%	10.624	2.86
	GZO–$Yb_{1\text{-sub}}$–$Sc_{1\text{-in+2-sub}}$	9.09%	3.03%	10.607	3.48
	GZO–$Yb_{1\text{-sub}}$–$Sc_{3\text{-sub}}$	9.38%	3.13%	10.597	11.78

As shown in Table 2, the Sc contents in GYbSc, GYbSc1, GYbSc2, and GYbSc3 are 5.88, 3.03, 5.88, and 8.57 at%, respectively. Combined with the solid solution mechanisms of Sc atoms in different compositions, it can be concluded that Sc atoms occupy interstitial sites in the GZO lattice when the Sc content is below 5.88 at%. When the Sc content ranges from 5.88 to 8.82 at%, Sc atoms tend to substitute for Gd. When Yb is present in the GZO lattice, Sc undergoes a transition from interstitial doping to substitutional doping at lower concentrations due to spatial competition between Yb and Sc. The substitution of Yb for Gd causes a contraction of the GZO lattice, compressing the availability of interstitial sites. This increases the difficulty for Sc to incorporate into the interstitial sites. When the Sc content exceeds 5.88 at%, the doping behavior shifts from being primarily interstitial to predominantly substitutional. Meanwhile, there is also a synergistic effect between Yb substitutional doping and Sc interstitial doping. When Yb replaces Gd, it leads to lattice contraction, whereas Sc interstitial doping can buffer this distortion through lattice expansion, and the strains cancel each other out, indirectly reducing the total energy of the composite defects and enhancing the stability of the lattice structure.

Figure 1(h) illustrates the variation in lattice parameters under different doping types and contents. As shown in this figure, the lattice parameter of GSc (10.649 Å) is larger than that of GZO (10.600 Å). The ionic radius of Sc^{3+} is 0.870 Å [39], and Sc incorporation into interstitial sites will lead to lattice expansion, which will increase the lattice parameters. In contrast, the lattice parameter of GYb (10.582 Å) decreases compared with that of GZO, as Yb is incorporated into the lattice via substitutional doping. The ionic radius of Yb^{3+} (0.985 Å) is smaller than that of Gd^{3+} (1.053 Å); therefore, the substitution of Gd^{3+} by Yb^{3+} leads to lattice contraction, thereby reducing the lattice parameter. The lattice constants of GSc and GYb can be calculated based on Vegard's law. GSc is regarded as Sc_2O_3 being added to GZO, and GYb is considered as part of GZO being replaced by $Yb_2Zr_2O_7$. The experimentally measured lattice constant of GZO is 10.52 Å, the lattice constant of Sc_2O_3 is 9.85 Å, and the lattice constant of $Yb_2Zr_2O_7$ is 10.22 Å. According to Vegard's law, the lattice constant of GSc is calculated to be 10.81 Å, and the lattice constant of GYb is 10.48 Å. This is consistent with the trend of the previous calculation results.

The lattice parameter of GYbSc is larger than that of GYb. By comparing GZO, GSc, and GYb, it can be observed that the lattice constant change caused by Sc interstitial doping is greater than that caused by Yb substitutional doping. This can be explained by the fact that, as shown in Fig. 1(d), the two Sc atoms in GYbSc are situated at the interstitial sites of the lattice, which generate a pronounced lattice expansion effect, ultimately leading to an increased lattice parameter compared with GYb. The lattice parameters of GYbSc1, GYbSc2, and GYbSc3 are all larger than those of GYb, which indicates that the lattice expansion effect caused by Sc interstitial doping is greater than that induced by Yb substitutional doping. In the GYbSc1 model, one Sc atom occupies an interstitial site, and three Yb atoms substitute for Gd atoms. The lattice expansion caused by Sc doping contributes to a larger lattice parameter of GYbSc1 compared with GYb. For the GYbSc2 model, two Sc atoms occupy interstitial sites, and two Yb atoms replace Gd atoms. Compared with GYbSc1, this composition results in weaker lattice contraction and stronger lattice expansion. Consequently, the lattice parameter of GYbSc2 is larger than that of GYbSc1. In the GYbSc3 model, two Sc atoms are located at interstitial sites, one Sc atom substitutes for Gd, and one Yb atom replaces Gd. Given that the ionic radius of Sc^{3+} (0.870 Å) is smaller than that of Yb^{3+} (0.985 Å), the substitution of Gd^{3+} by Sc^{3+} gives rise to a more pronounced lattice contraction. Consequently, the lattice parameter of GYbSc3 is smaller than that of GYbSc2. The synergistic effect between Yb substitutional doping and Sc interstitial doping enhances the stability of the lattice. As shown in Fig. 1(h), the lattice constant of GYb decreases sharply, while that of GSc increases sharply. The lattice constant of GYbSc–GYbSc3 lies between those of GYb and GSc. This is because the radius of Yb^{3+} is smaller, and Yb^{3+} substitution for Gd^{3+} leads to lattice contraction. Sc atoms enter the interstitial sites of GZO, causing lattice expansion. When both Yb^{3+} and Sc^{3+} coexist in the GZO lattice, the lattice contraction caused by the substitution of Yb^{3+} can be alleviated by the lattice expansion

caused by the interstitial doping of Sc. The strains produced by both partially cancel each other out, thereby enhancing the stability of the lattice structure.

3.2 Theoretical prediction of mechanical and thermophysical properties of doped GZO compounds

Based on the optimized structures, the mechanical properties of GZO, GSc, GYb, GYbSc, and GYbSc1–3 were calculated, including elastic constants (C_{ij}), bulk modulus (B), shear modulus (G), and Young's modulus (E). The GZO crystal has a cubic structure, which has three independent elastic constants: C_{11}, C_{12}, and C_{44} [24]. Figure 2(a) shows that the elastic constants of GSc and GYb are lower than those of GZO. Compared with GYb, the elastic constants C_{11} and C_{44} of GYbSc decrease, while C_{12} increases. All elastic constants of GYbSc1–3 are greater than those of GYb. From GYbSc1 to GYbSc3, the Yb content decreases while the Sc content increases. During this compositional transition, the elastic constants C_{11} and C_{12} exhibit a gradual increase, whereas C_{44} shows a continuous decrease. The reduction in the values of the three elastic constants indicates that the material's resistance to external stress is weakened, and the crystal as a whole becomes "soft" [40]. For TBC materials, the reduction in elastic constants can enhance the strain tolerance of the material, absorb strain generated by thermal expansion mismatch via minor deformation, reduce the accumulation of thermal stress, and thereby improve the thermal shock resistance of the coating. GYbSc exhibits the lowest values of C_{11} (236.863 GPa) and C_{44} (47.116 GPa), coupled with a relatively low C_{12} (78.361 GPa), thus endowing it with superior mechanical properties. However, a reduction in the elastic modulus compromises the material's hardness, thereby increasing its susceptibility to surface damage induced by airborne contaminants or abrasive particles and ultimately undermining the structural integrity of the coating. Section 3.3 will further explore the influence of dopant incorporation on the material's hardness. For cubic crystals, the elastic constants C_{11}, C_{12}, and C_{44} must satisfy Eq. (2) to ensure the mechanical stability of the structure [24]. According to the calculation results in Table S1 in the ESM, the GZO, GSc, GYb, GYbSc, and GYbSc1–3 models all exhibit stable structures.

The variation trend of the elastic modulus for GZO, GSc, GYb, GYbSc, and GYbSc1–3 is shown in Fig. 2(b), with the corresponding values listed in Table S1 in the ESM. It is evident that the E, B, and G of GSc and GYb are lower than those of GZO; additionally, the elastic modulus of GYbSc is smaller than that of GYb. The difference in ionic radii between the dopant and host ions leads to lattice size mismatch and local strain field fluctuations, which weaken the interatomic bonding and result in lattice softening [40]. The further incorporation of Sc into GYb exacerbates lattice distortion, which in turn contributes to a further reduction in the elastic modulus. The elastic moduli of GYbSc1–3 are higher than those of GYb. From GYbSc1 to GYbSc3, the changes in E and G are relatively small, while B increases gradually.

The thermal stress resistance of TBCs depends not only on their microstructure and porosity but also on the E of the coating material [41,42]. In the working environment of aeroengines, a lower E can effectively reduce the residual thermal stress of the coating, thereby enhancing the thermal mechanical stability and thermal shock resistance of the coating. A lower B typically indicates that the material possesses lower rigidity and greater elastic deformation, which can contribute to higher toughness and a larger thermal expansion coefficient for the coating [43]. A lower G indicates that the material is more prone to elastic deformation rather than brittle fracture under shear loading, thereby effectively reducing stress concentration within the coating [44]. In addition, a lower shear modulus decreases the stress intensity factor at the crack tip and increases the resistance to crack propagation. This effectively delays the premature failure of the coating and extends its service life. Since GYbSc exhibits the lowest values of E (151.888 GPa), B (131.195 GPa), and G (58.104 GPa), it is expected to possess optimal mechanical properties.

Figure 2(c) presents the variation trends of G/B and σ for GZO, GSc, GYb, GYbSc, and GYbSc1–3. As seen from the figure, the G/B values of GSc and GYb are smaller than those of GZO, while the σ values of GSc and GYb are higher than those of GZO. The G/B value of GYbSc is lower than that of GYb, and the σ value is higher than that of GYb. From GYbSc1 to GYbSc3, as the Sc content increases, G/B gradually decreases, and σ gradually increases. Table S2 in the ESM presents the calculation results of G/B and σ for different doped systems. The G/B and σ of GZO are 0.543 and 0.270, respectively, which agree well with the experimental results reported in Refs. [18,28]. According to Pugh's empirical criterion, materials with a G/B ratio below 0.57 are classified as ductile materials and tend to release external stress through plastic deformation rather than fracture. In contrast, materials with a G/B ratio exceeding 0.57 are classified as brittle materials, which possess a stronger resistance to shape changes but are more prone to brittle fracture [45]. Poisson's ratio (σ), also known as the lateral deformation coefficient, is used to reflect the lateral deformation capacity of a material under tension or compression. Previous research indicates that σ can serve as an indicator to distinguish between ductile and brittle materials, with a critical value of 0.26. When the Poisson's ratio is lower than 0.26, the material is brittle; when it is higher than 0.26, the material is ductile [46,47]. Moreover, the higher the Poisson's ratio is, the better the toughness of the material is. GYbSc3 exhibits the lowest G/B ratio (0.415) and the highest σ (0.318), thus possessing the optimal fracture toughness; by comparison, GYbSc also demonstrates favorable fracture toughness, with corresponding G/B and σ values of 0.443 and 0.307, respectively.

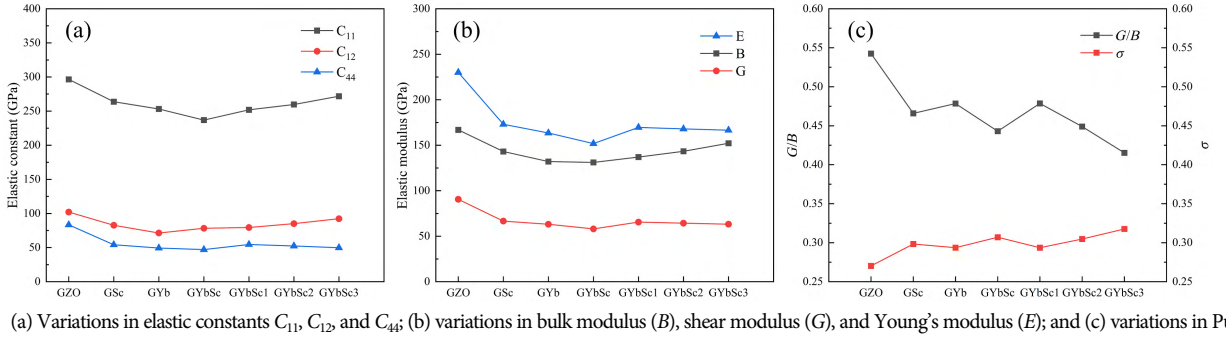

Fig. 2 (a) Variations in elastic constants C_{11}, C_{12}, and C_{44}; (b) variations in bulk modulus (B), shear modulus (G), and Young's modulus (E); and (c) variations in Pugh's indicator (G/B) and Poisson's ratio (σ).

Figure 3(a) presents the thermal conductivity of various materials calculated using the Clarke and Cahill models [33–35]. The simulation results demonstrate that the thermal conductivities of GSc and GYb are lower than that of GZO, with GYb exhibiting a comparatively lower thermal conductivity. The incorporation of Sc into GYb, yielding GYbSc, causes the lowest thermal conductivity among the studied systems. In addition, the thermal conductivities of GYbSc1–3 are all higher than that of GYb; with the decrease in Yb content, the thermal conductivity slightly increases. Table S3 in the ESM lists the longitudinal acoustic velocity v_l, transverse acoustic velocity v_t, and average acoustic velocity v_m of GZO, GSc, GYb, GYbSc, and GYbSc1–3, along with the corresponding thermal conductivity values calculated via the Clarke and Cahill models. As seen from the table, the doping of rare earth elements leads to a significant reduction in the sound velocity of GZO. Both the interstitial doping of Sc and Yb substitution for Gd introduce point defects, which induce lattice distortion, enhance phonon scattering, and reduce phonon propagation velocity, thereby lowering the thermal conductivity of the material [33,48]. The phonon scattering process caused by lattice distortion can be reflected by the phonon-defect scattering relaxation time, as shown in Eqs. (18)–(20) [49]:

$$\tau_D^{-1} = A\omega^4 \tag{18}$$

$$A = \frac{\Omega\Gamma}{4\pi v_s^3} \tag{19}$$

$$\Gamma_i = f_i\left\{\left(\frac{\Delta M_i}{M}\right)^2 + 2\left[6.4\cdot\frac{1}{3}\gamma\frac{1+\sigma}{1-\sigma}\left(\frac{\Delta R_i}{R}\right)\right]\right\} \tag{20}$$

where ω is the phonon frequency, and Ω is the average volume per atom. Γ is the phonon scattering coefficient, and v_s is the average sound velocity. The subscript i represents a certain kind of lattice defect and f_i is the fractional concentration of them. M and R are the average value of the atomic mass and the ionic radius at the corresponding defective crystalline site. $\Delta M_i = M - M_i$ and $\Delta R_i = R - R_i$, where M_i and R_i represent the atomic mass and ionic radius of the defect, respectively. γ is the Grüneisen parameter and σ is the Poisson's ratio. The ionic radii of Gd^{3+}, Yb^{3+}, and Sc^{3+} are 1.053, 0.985, and 0.870 Å, respectively, and their relative atomic masses are 157.25, 173.05, and 44.956. Differences exist in both the mass and ionic radius between Yb^{3+} and Gd^{3+}. The substitution of Yb^{3+} for Gd^{3+} in the GZO lattice induces lattice distortion and intensifies phonon scattering. The difference in mass and ionic radius between Sc^{3+} and Gd^{3+} is even greater. As the doping mode of Sc is interstitial doping, it will bring greater lattice distortion. This also leads to a further reduction in the thermal conductivity of the material. However, the interstitial doping of Sc will reduce the number of oxygen vacancies in the lattice, which limits the reduction in thermal conductivity to a certain extent. This point requires further in-depth research.

GYbSc is derived from GYb with an additional 5.88% Sc doping, and this modification increases the total doping content and the degree of lattice distortion in the system, further intensifying phonon scattering. The enhanced phonon scattering could shorten the average free path of phonons, ultimately causing the material to exhibit extremely low thermal conductivity. From GYbSc1 to GYbSc3, the Yb content decreases while the Sc content increases, with the total doping concentration remaining at 12.5%. Consequently, the degree of lattice distortion induced by doping is similar across these materials. The thermal conductivity increases slightly from GYbSc1 to GYbSc3. GYbSc exhibits the lowest thermal conductivity among the studied compositions, and the thermal conductivity values calculated using the Cahill and Clarke models are 1.01 and 1.12 $W\cdot m^{-1}\cdot k^{-1}$, respectively.

As shown in Fig. 3(b), GSc and GYb exhibit lower Debye temperatures (Θ) and higher CTE than GZO. Compared with GYb, GYbSc exhibits a lower Debye temperature and a higher CTE. The Debye temperatures and CTE of GYbSc1, GYbSc2, and GYbSc3 show little variation. Table S4 in the ESM presents the calculated Debye temperatures and CTE of different materials. The Debye temperature is an important physical parameter of solid materials and is derived from the theory of atomic vibration in solids. The Debye temperature not only reflects the degree of dynamic distortion of the crystal lattice but also indicates the strength of the interatomic bonds [31]. The lower the interatomic interaction forces are, the weaker the constraint on the atomic vibration is, the lower the characteristic vibration frequency is, and the lower the Debye temperature is. Therefore, a lower Θ indicates weaker atomic interactions within the lattice, which in turn leads to a higher CTE. Figure 3(b) shows that GYbSc has the lowest Debye temperature and the highest CTE, with values of 408.989 K and 14.339×10^{-6} K^{-1}, respectively.

Although the first-principles calculation results show certain deviations from the experimental results, the overall trend is consistent with the experimental results. In conclusion, GYbSc exhibits the lowest thermal conductivity, the highest CTE, and relatively favorable fracture toughness. GYb has a relatively low thermal conductivity and a high coefficient of thermal expansion, and GYbSc was developed based on this composition. Therefore, GYb and GYbSc were selected for subsequent experiments.

3.3 Mechanical and thermophysical properties of GZO, GYb, and GYbSc

Figure 4(a) shows the XRD patterns of GZO, GYb, and GYbSc.

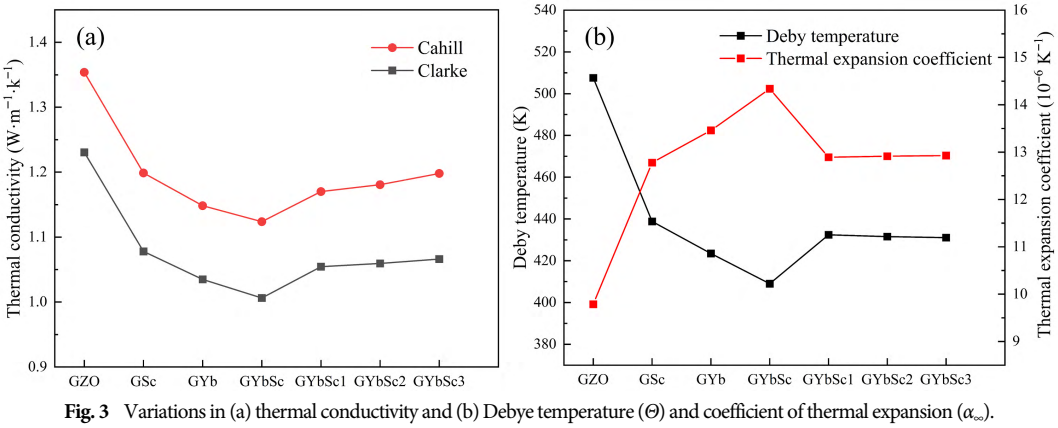

Fig. 3 Variations in (a) thermal conductivity and (b) Debye temperature (Θ) and coefficient of thermal expansion (α_∞).

The results indicate that the diffraction peaks of the GZO pellet match those of PDF card #80-0470, with characteristic peaks at 28° (311), 37° (331), and 44° (511), confirming that GZO has a pyrochlore structure. The diffraction peaks presented by GYb and GYbSc correspond to those of PDF card#80-0471, indicating that GYb and GYbSc have a defect fluorite structure. Meanwhile, the positions of the peaks corresponding to the (111) crystal plane of GZO, GYb, and GYbSc are 29.46°, 29.49°, and 29.30°, respectively. The diffraction peaks of GYb shift toward higher angles, indicating a decrease in the lattice parameter. The diffraction peaks of GYbSc shift toward lower angles, indicating an increase in the lattice parameter. This result is consistent with the simulation results. Figures 4(b) and 4(c) show the XRD patterns of the GYb and GYbSc materials after heat treatment at 1400 °C for different times. It can be seen from the figures that no phase transformation occurs in the two materials during long-term high-temperature heat treatment, indicating that GYb and GYbSc have excellent high-temperature phase stability at 1400 °C.

Figure 5(a) shows the hardness of GZO, GYb, and GYbSc. The corresponding values are 7.72, 9.91, and 12.76 GPa, respectively. The results indicate that both GYb and GYbSc exhibit improved hardness compared with GZO. The fracture toughness results are shown in Fig. 5(b), with the inset illustrating the indentation morphology. The fracture toughness values of GZO, GYb, and GYbSc are 1.04, 1.85, and 2.09 MPa·m$^{1/2}$, respectively. Higher hardness and fracture toughness ensure the structural integrity of the coating during service. The enhancement of hardness in GYb and GYbSc can be analyzed from two aspects: solid solution strengthening and grain refinement effect. The ionic radii of Yb^{3+}, Sc^{3+}, and Gd^{3+} are different. The entry of Yb^{3+} and Sc^{3+} into the GZO lattice will cause lattice distortion. Lattice distortion increases the resistance to dislocation movement, making slip difficult to occur and thereby enhancing the hardness of the material [50]. On the other hand, doped elements can inhibit grain growth, leading to grain refinement. Grain boundaries act as obstacles to dislocation movement, and a finer grain structure significantly enhances the material's hardness. As shown in Figs. 5(c)–5(e), both GYb and GYbSc exhibit smaller grains, resulting in higher hardness. This increased hardness helps maintain the structural integrity of the coating during use.

The change in σ and grain refinement caused by doping can also affect the fracture toughness of the material. According to first-principles calculation results, doping with Yb and Sc increases the σ of the material. A higher σ implies that the material exhibits enhanced lateral deformation coordination under loading, which can effectively reduce the stress concentration at the crack tip,

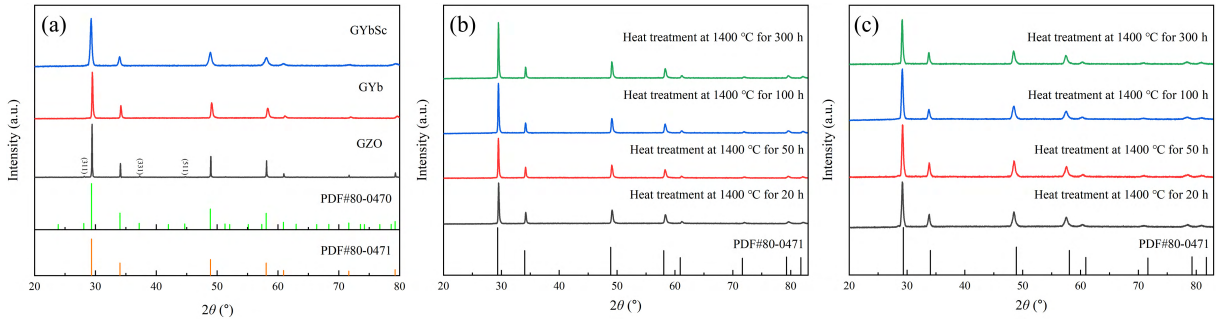

Fig. 4 XRD patterns of (a) GZO, GYb, and GYbSc; (b) GYb; and (c) GYbSc after heat treatments at 1400 °C for 20, 50, 100, and 300 h.

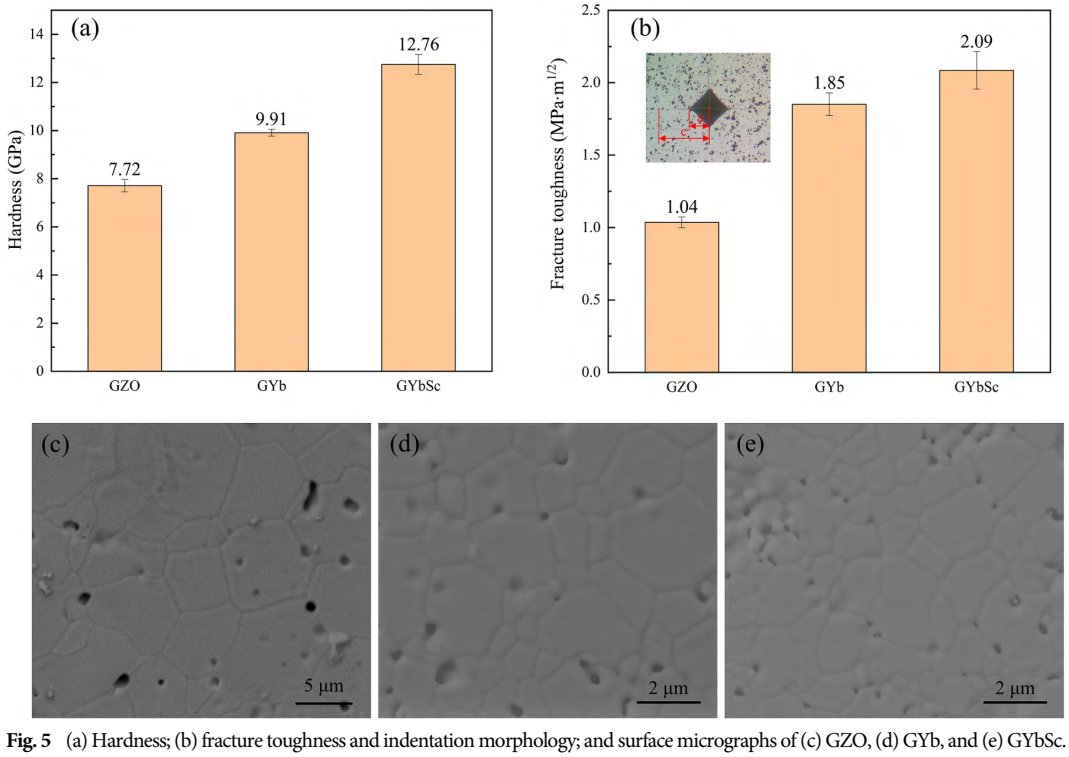

Fig. 5 (a) Hardness; (b) fracture toughness and indentation morphology; and surface micrographs of (c) GZO, (d) GYb, and (e) GYbSc.

blunt the crack tip, reduce the stress field mutation, and inhibit the rapid expansion of the crack. The grain refinement of GYb and GYbSc significantly increases the number and total length of grain boundaries. As effective barriers to crack propagation, grain boundaries cause the crack to constantly deviate, bridge, and bifurcate during propagation, change the expansion path, and increase the roughness of the fracture surface, thereby significantly enhancing the energy dissipation during fracture. At the same time, a greater density of grain boundaries disperses stress concentrations, alleviates local stress overload, and inhibits the rapid instability and expansion of cracks. Thus, the fracture toughness of GYb and GYbSc is higher than that of GZO, and GYbSc exhibits the highest fracture toughness, which is consistent with the trend of calculation results discussed earlier.

As mentioned earlier, Yb doping induces a phase transition in GZO, from the ordered pyrochlore structure to the disordered defect-fluorite structure. The fracture toughness of ceramic materials is generally proportional to the cohesive energy within the lattice, while lattice distortion and structural disorder can increase the lattice cohesive energy [50]. The lattice distortion and phase transition induced by Yb doping increase the cohesive energy of the GYb lattice compared with that of GZO, thereby enhancing its fracture toughness. With the introduction of Sc into GYb, the fracture toughness of GYbSc is further improved through two main mechanisms. On the one hand, the phase transition and lattice distortion contribute to enhanced fracture toughness; on the other hand, interstitial Sc doping reduces the concentration of oxygen vacancies in the lattice, which further improves the fracture toughness of GYbSc. High concentrations of oxygen vacancies can disrupt the integrity of the lattice, reducing the energy required to form new fracture surfaces and lowering the fracture toughness of the material [51]. During the interstitial doping process of Sc, oxygen vacancies are consumed to maintain charge balance in the system, thereby further improving the fracture toughness of GYbSc.

Figures 5(c)–5(e) show the microstructure images of the surfaces of GZO, GYb, and GYbSc. These figures show that the grain size of GZO is approximately 5–10 μm, the grain size of GYb is approximately 2–4 μm, and the grain size of GYbSc is approximately 1–3 μm. This suggests that GYb and GYbSc possess superior sintering resistance. Sintering is essentially a mass diffusion process. The differences in ionic radii between Yb^{3+} and Gd^{3+} induce lattice distortion and generate strain fields. The distorted lattice requires atoms to overcome higher energy barriers for migration, which further retards atomic diffusion during sintering, thereby inhibiting grain growth and densification [50]. The incorporation of Sc into GYb further enhances lattice distortion, thereby enabling GYbSc to exhibit superior sintering resistance.

Figure 6(a) presents the measured CTE of GZO, GYb, and GYbSc. As shown, both GYbSc and GYb exhibit relatively higher CTE than GZO. At 1300 °C, the CTE values of GYbSc and GYb are 11.059×10^{-6} and 10.827×10^{-6} K^{-1}, respectively. It has been reported that the CTE of a material is related to the strength of its ionic bonds: materials with weaker ionic bonds tend to have higher CTE values. The ionic bond strength within the crystal can be calculated using Eq. (21) [52,53]:

$$I_{A\text{-}B} = 1 - e^{-\frac{(x_A - x_B)^2}{4}} \quad (21)$$

where $I_{A–B}$ represents the ionic bond strength between the cation and anion sites, while x_A and x_B correspond to the average electronegativities of the cation and anion sites, respectively. The electronegativities of Gd, Sc, Yb, Zr, and O are 1.22, 1.36, 1.26, 1.33, and 3.44, respectively. The ionic bond strength ($I_{A–B}$) for GZO is 0.6902, for GYb is 0.6895, and for GYbSc is 0.6872. Therefore, GYb and GYbSc exhibit higher CTE than GZO, and GYbSc shows the highest CTE, which is consistent with the trend of the previously calculated results.

Figure 6(b) presents the test results of the thermal diffusivity of GZO, GYb, and GYbSc. All the curves show a good temperature dependence, and the thermal diffusivity gradually decreases with increasing temperature. The thermal diffusivity of GYb and GYbSc is significantly lower than that of GZO. The thermal diffusivities of GZO, GYb, and GYbSc at 1200 °C are 0.39, 0.29, and 0.27 $mm^2 \cdot s^{-1}$, respectively. The thermal diffusivities of GYb and GYbSc show minimal differences, which may be because while the interstitial doping of Sc_2O_3 increases the lattice distortion, it simultaneously reduces the concentration of oxygen vacancies. As a result, the change in thermal diffusivity of GYbSc is relatively small compared with that of GYb. The thermal conductivity (λ) of the samples is determined by the product of the thermal diffusivity (k), specific heat capacity (c_p), and density (ρ), as given by Eq. (22):

$$\lambda = k \cdot c_p \cdot \rho \quad (22)$$

Figure S3 in the ESM shows the measured specific heat capacities of GYb and GYbSc. Figure 6(c) shows the temperature dependence of the thermal conductivity of GZO, GYb, and GYbSc, calculated from the specific heat capacity, thermal diffusivity, and density test results. The thermal conductivity of GYb and GYbSc is significantly lower than that of GZO, with GYbSc exhibiting the lowest values, which is consistent with the trend of the calculated results. At 1200 °C, the thermal conductivities of GYb and GYbSc are 0.999 and 0.935 $W \cdot m^{-1} \cdot K^{-1}$, respectively, which are lower than that of GZO of 1.50 $W \cdot m^{-1} \cdot K^{-1}$ [54].

The thermal conduction process of ceramic materials can be described relatively accurately through phonon theory. Lattice defects introduced by substitutional doping or interstitial doping are important phonon scattering centers. These defects not only intensify phonon scattering but also enhance the anharmonicity of

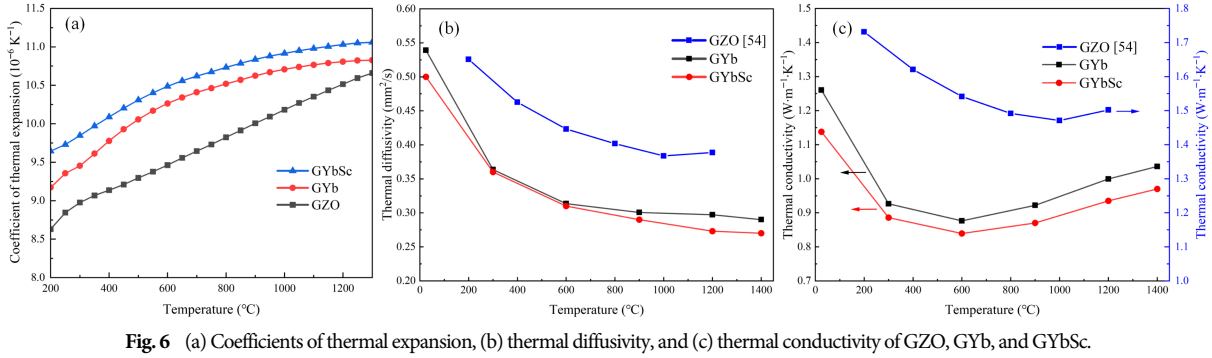

Fig. 6 (a) Coefficients of thermal expansion, (b) thermal diffusivity, and (c) thermal conductivity of GZO, GYb, and GYbSc.

lattice vibrations, thereby increasing the intrinsic scattering between phonons [55,56]. The point defects produced by Yb doping and Yb–Sc codoping intensify phonon scattering, thereby enabling GYb and GYbSc to achieve lower thermal conductivity. On the other hand, doping can affect the average free path of phonons. It is influenced by crystal defects, impurities, and the interaction between phonons, and it is an important factor in determining the thermal conductivity of materials. The average free path of phonons is directly proportional to the relaxation time. The effect of the mass difference between dopant atoms and substrate atoms and the variation in interatomic distances on the relaxation time can be expressed as Eqs. (23) and (24) [57,58]:

$$\frac{1}{\tau_M(\omega)} = \frac{\Omega c\omega^4}{4\pi v^3}\left(\frac{\Delta M_a}{M_a}\right)^2 \tag{23}$$

$$\frac{1}{\tau_R(\omega)} = \frac{2\Omega c\omega^4}{\pi v^3} J^2\gamma^2\left(\frac{\Delta R}{R}\right)^2 \tag{24}$$

where $\tau_M(\omega)$ and $\tau_R(\omega)$ represent the influence of mass change and interatomic spacing change on the relaxation time. M represents the mass of the matrix atoms, and ΔM_a represents the mass difference between the doped atoms and the matrix atoms. R represents the interatomic spacing of the matrix atoms, and ΔR represents the change in interatomic spacing caused by doping. Ω is the average volume of atoms, and c is the defect concentration. v represents the velocity of the transverse phonon; γ is the Grüneisen constant; J is a constant independent of the material. The ionic radius of Yb^{3+} is smaller than that of Gd^{3+}, while its mass is greater than that of Gd^{3+}. According to the above formula, Yb doping reduces the phonon relaxation time, thereby decreasing the mean free path of phonons, resulting in a lower thermal conductivity for GYb. With the introduction of Sc into GYb, the ionic radius of Sc^{3+} is smaller than that of Gd^{3+}, and its mass is also smaller than that of Gd^{3+}. The mass difference and radius mismatch between Sc^{3+} and Gd^{3+} further shorten the phonon relaxation time, thereby reducing the phonon mean free path and intensifying phonon scattering. As a result, GYbSc exhibits an even lower thermal conductivity.

In summary, GYbSc exhibits superior mechanical properties, sintering resistance, and thermophysical performance compared with GZO and GYb. The hardness and fracture toughness of GYbSc reach 12.76 GPa and 2.09 $MPa{\cdot}m^{1/2}$, respectively. At 1300 °C, GYbSc shows a coefficient of thermal expansion of 11.059×10^{-6} K^{-1}, while at 1200 °C, its thermal diffusivity and thermal conductivity are 0.27 $mm^2{\cdot}s^{-1}$ and 0.935 $W{\cdot}m^{-1}{\cdot}K^{-1}$, respectively.

3.4 Comparison of CMAS resistance among GZO, GYb, and GYbSc

To obtain the melting point of CMAS, a DSC test was carried out, and the test result is shown in Fig. 7(a), in which three exothermic peaks and one endothermic peak are observed during the test. The exothermic peaks at 838 and 992 °C have relatively low intensities, indicating low crystallinity and the formation of a small amount of crystalline phase at these temperatures. The exothermic peak at 946 °C has a higher intensity, suggesting a higher degree of CMAS crystallization at this temperature. By observing the variation in the endothermic peak, the CMAS began to melt at 1134 °C and was completely melted at 1220 °C. To study the crystalline phases formed by CMAS corresponding to different exothermic peaks, the CMAS samples were heat-treated at 838, 946, and 992 °C. Figure 7(b) shows the macroscopic morphology of the material after holding at different temperatures. The CMAS does not melt under the three temperature conditions. The XRD test results are shown in Fig. 7(c). Only a small amount of crystalline phase formed at 838 °C, and the main phase was spinel. As the temperature increased to 946 °C, the newly formed phases included anorthite and diopside. At 992 °C, the newly formed phase was wollastonite.

Figures 8(a)–8(c) show the cross-sectional microstructure, the corresponding EDS mappings, and magnified images of the reaction layer of the GZO material after 10 h of exposure to CMAS at 1250 °C, respectively. It can be observed that there is little residual CMAS on the surface of the GZO sample, and the reaction layer has a thickness of approximately 66.8 μm. A large number of elements, such as Ca and Si, which originated from CMAS, were detected in this reaction layer, indicating that CMAS has completely permeated into the interior of the GZO material. Table S5 in the ESM shows the elemental composition of compounds at different sites in the cross-sections of GZO

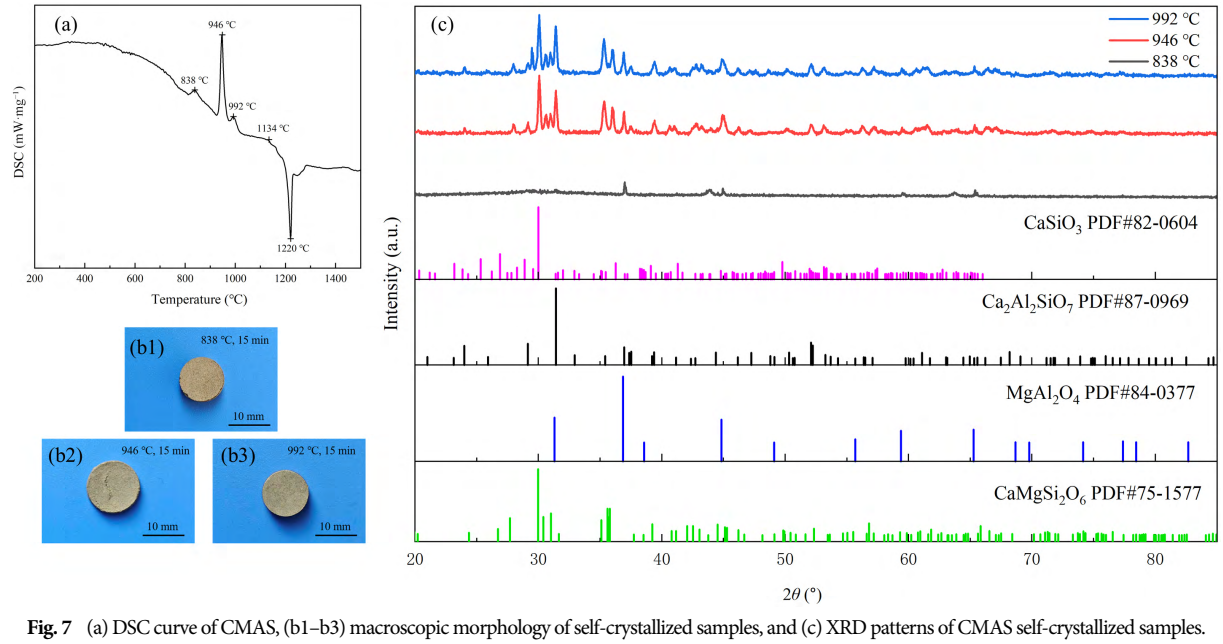

Fig. 7 (a) DSC curve of CMAS, (b1–b3) macroscopic morphology of self-crystallized samples, and (c) XRD patterns of CMAS self-crystallized samples.

(Fig. 8(c)), GYb (Fig. 8(f)), and GYbSc (Fig. 8(i)). Figures 8(d) and 8(e) show the cross-sectional microstructure and corresponding EDS mapping analysis of the GYb sample exposed to CMAS for 10 h. As shown in Fig. 8(d), only a small amount of CMAS remains on the sample surface, and the thickness of the reaction layer is approximately 58.4 μm. Figures 8(g) and 8(h) show the cross-sectional microstructure and EDS mappings of GYbSc exposed under the same conditions. The results show that the surface of GYbSc remains a relatively thick residual CMAS layer, with a reaction layer thickness of approximately 42 μm.

With the heat-treatment time extended to 15 h, some CMAS remained on the surface of GYbSc, whereas the CMAS on the surfaces of the GZO and GYb samples nearly completely reacted. To study the corrosion behavior of GZO, GYb, and GYbSc and their reaction products in the CMAS environment, XRD analysis was performed on the surface of the samples, and the results are shown in Fig. 9. The surface of the samples primarily contains a ZrO_2-based fluorite phase and $Gd_8Ca_2Si_6O_{26}$-based apatite phase generated by the corrosion reaction and spinel and melilite phases formed by CMAS crystallization. Combined with the point-scan results and XRD phase analysis, the marked regions A, B, and C in Fig. 8(c) could be identified as the fluorite, apatite, and spinel phases, respectively. Figure 8(f) shows the reaction layer of GYb, in which regions A, B, and C correspond to the fluorite, apatite, and spinel phases, respectively. The phases corresponding to marked points A, B, C, and D in Fig. 8(i) are identified as fluorite, apatite, spinel, and melilite phases, respectively.

The reaction layer in Figs. 8(a), 8(d), and 8(g) can be roughly divided into three parts: The upper layer consists of loosely packed, rod-like apatite, and spherical fluorite; the middle layer contains incompletely grown apatite, fluorite, and infiltrated CMAS; and the bottom layer consists of a dense reaction layer. According to the sequence of GZO, GYb, and GYbSc, the particle size of apatite and fluorite in the upper layer gradually increases, while the quantity of the reaction layer products decreases. The reactivity of Gd, Yb, and Sc with environmental deposits gradually decreases, Gd and Yb diffuse outward, a large amount of apatite and fluorite nucleate, and eventually form a large number of reaction products with small particle sizes. The relatively low reactivity of Sc limits the diffusion of Gd, Yb, and Zr, resulting in a reduced number of nucleation sites for both apatite and fluorite phases. Consequently, sufficient growth of the apatite and fluorite phases occurs in the reaction layer of GYbSc, resulting in the formation of an upper reaction layer with fewer reaction products and larger grain sizes.

The concept of optical basicity (OB) was first proposed by

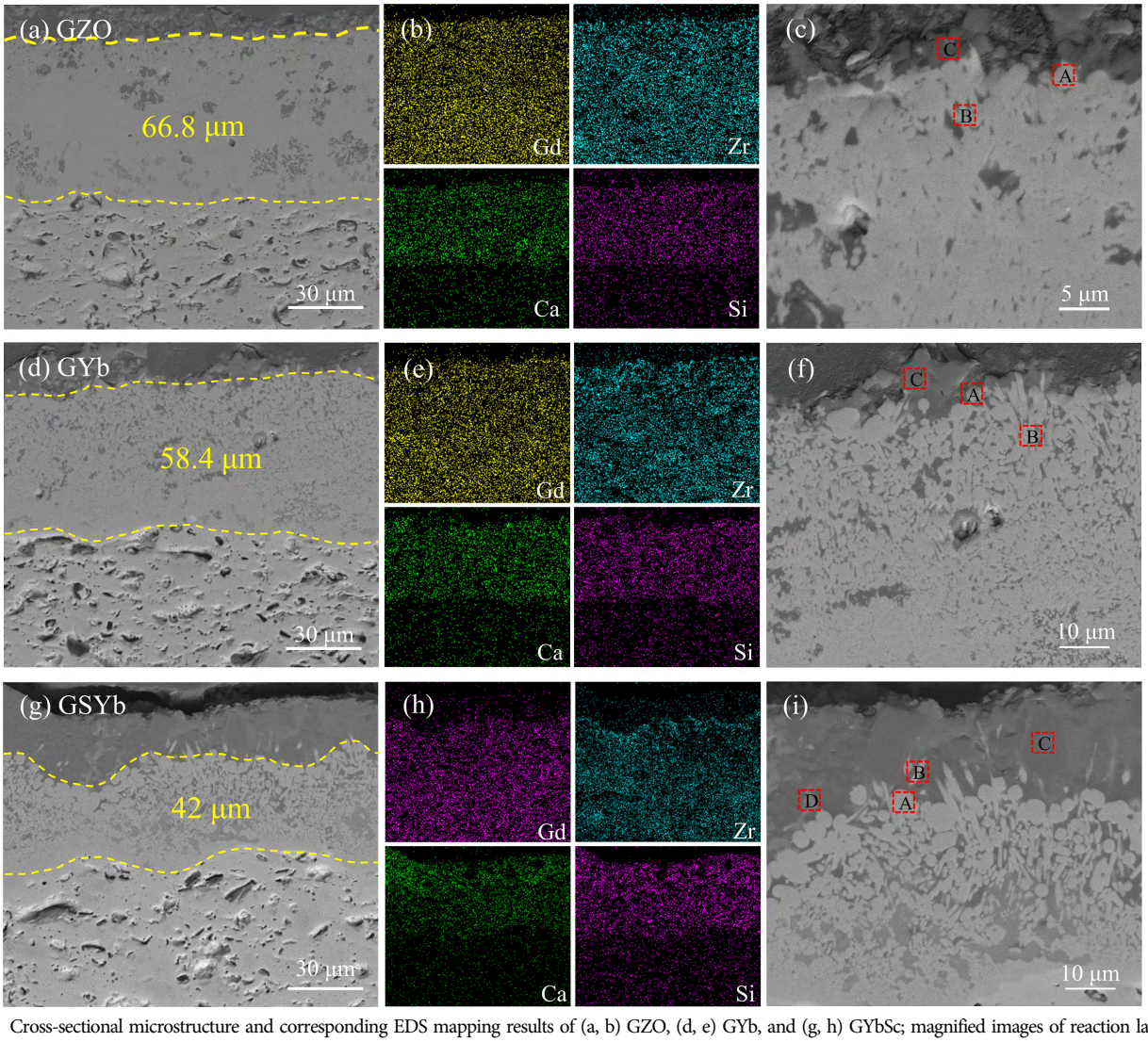

Fig. 8 Cross-sectional microstructure and corresponding EDS mapping results of (a, b) GZO, (d, e) GYb, and (g, h) GYbSc; magnified images of reaction layer of (c) GZO, (f) GYb, and (i) GYbSc after exposure to CMAS at 1250 °C for 10 h.

Duffy [59]. Based on Lewis acid-base theory to describe the electron-donating and electron-accepting capabilities of oxide ions. For TBC materials, OB can be used to evaluate the chemical reactivity between molten environmental deposits and TBC materials. A greater difference in OB between the two materials indicates higher chemical reactivity, making the coating more susceptible to reaction with environmental deposits. For CMAS and TBC materials composed of multiple components, their OB can be calculated using Eq. (25) [59–61]:

$$\Lambda = (X_A \times \Lambda_A) + (X_B \times \Lambda_B) + (X_C \times \Lambda_C) + \ldots \quad (25)$$

where X_A, X_B, and X_C represent the fractions of oxygen ions contributed by oxides A, B, and C, respectively. Λ_A, Λ_B, and Λ_C are the OB values of each oxide. According to this formula, the OB of CMAS, GZO, GYb, and GYbSc can be calculated as 0.69, 1.16, 1.15, and 1.14, respectively. This suggests that compared with GZO, GYb and GYbSc have lower chemical reactivity with CMAS, and GYbSc reveals the weakest reactivity toward CMAS. The low optical basicity of Sc_2O_3 leads to a decrease in the optical basicity of GYbSc. This reduces the gap between the optical basicities of GYbSc and CMAS, thereby lowering the reactivity of GYbSc with CMAS. Therefore, the reaction layer formed by GZO and CMAS is the thickest, while the reaction layer formed by GYbSc and CMAS is the thinnest. GYbSc effectively inhibits the diffusion and penetration of CMAS.

Based on the above results, CMAS (with a density of 10 mg·cm^{-2}) was uniformly coated on the surface of the samples again and placed in a high-temperature environment of 1250 °C for 10 min, 5 h, and 10 h to further investigate their high-temperature corrosion behavior. Figure 10 shows the cross-sectional morphology of the materials and the EDS mappings of some elements after 10 min of heat treatment. The residual CMAS thicknesses on the surfaces of GZO, GYb, and GYbSc are 51.6, 51.6, and 65.2 μm, respectively, while the thicknesses of the reaction layer are 82.4, 73.2, and 66.4 μm, respectively. The GZO and GYb samples exhibit obvious CMAS penetration, and the thickness of the residual layer on their surfaces is less than that of the GYbSc samples. EDS mappings revealed significant diffusion of Gd and Yb in both the residual layer and the reaction layer. In contrast, the diffusion of Sc is limited, with no significant accumulation observed in either the reaction layer or the residual layer. This result is consistent with the previously observed microstructural features of the reaction layer, further explaining the relatively thinner reaction layer in the GYbSc sample.

Figure 11 shows the thickness of the residual CMAS layer and the reaction layer formed by the reactions of GZO (Fig. 11(a)), GYb (Fig. 11(b)), and GYbSc (Fig. 11(c)) with CMAS at different heat treatment times following the secondary CMAS coating. With the extension of heat treatment time, the thickness of the reaction layers of the three materials gradually increases. As the corrosion time extends from 10 min to 10 h, the reaction layer thickness between GZO and CMAS increases from 83 to 117.4 μm, with virtually no residual CMAS remaining on the surface after 10 h. For GYb, the reaction layer thickness increases from 72.7 to 105.7 μm, with approximately 30 μm of residual CMAS remaining on the surface after 10 h. For GYbSc, the reaction layer thickness increases from 68.9 to 95.8 μm, with approximately 36 μm of residual CMAS remaining on the surface after 10 h. Among the three materials, GZO exhibits the most significant increase in reaction layer thickness, while GYbSc shows the smallest increment.

In summary, both GYb and GYbSc exhibit better resistance to CMAS corrosion than GZO, with GYbSc demonstrating the best performance. Sc has extremely low reactivity with environmental deposits and does not form apatite. Its weak diffusion ability in CMAS helps to enhance the interfacial stability of GYbSc, thereby endowing it with optimal corrosion resistance.

4 Conclusions

In this study, first-principles calculations are used to study the solid solution mechanism of Yb in the GZO lattice and Sc in the Yb-doped GZO lattice. The mechanical and thermophysical properties of GZO, Yb-doped GZO, and Yb–Sc codoped GZO were calculated. Based on the calculation results, GYb and GYbSc were selected for experimental verification. Their mechanical and thermophysical properties were systematically tested, and their corrosion resistance in the CMAS environment was studied. The main conclusions are as follows:

(1) First-principles calculations reveal that at a Yb doping concentration of 12.5 at%, Yb substitutes for Gd in the GZO

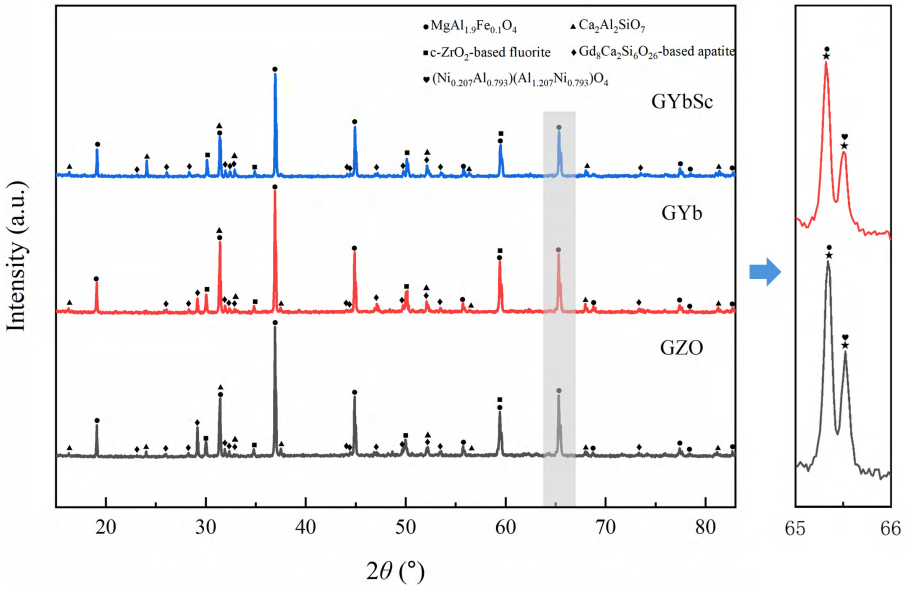

Fig. 9 XRD patterns of GZO, GYb, and GYbSc covered with CMAS at 1250 °C for 15 h.

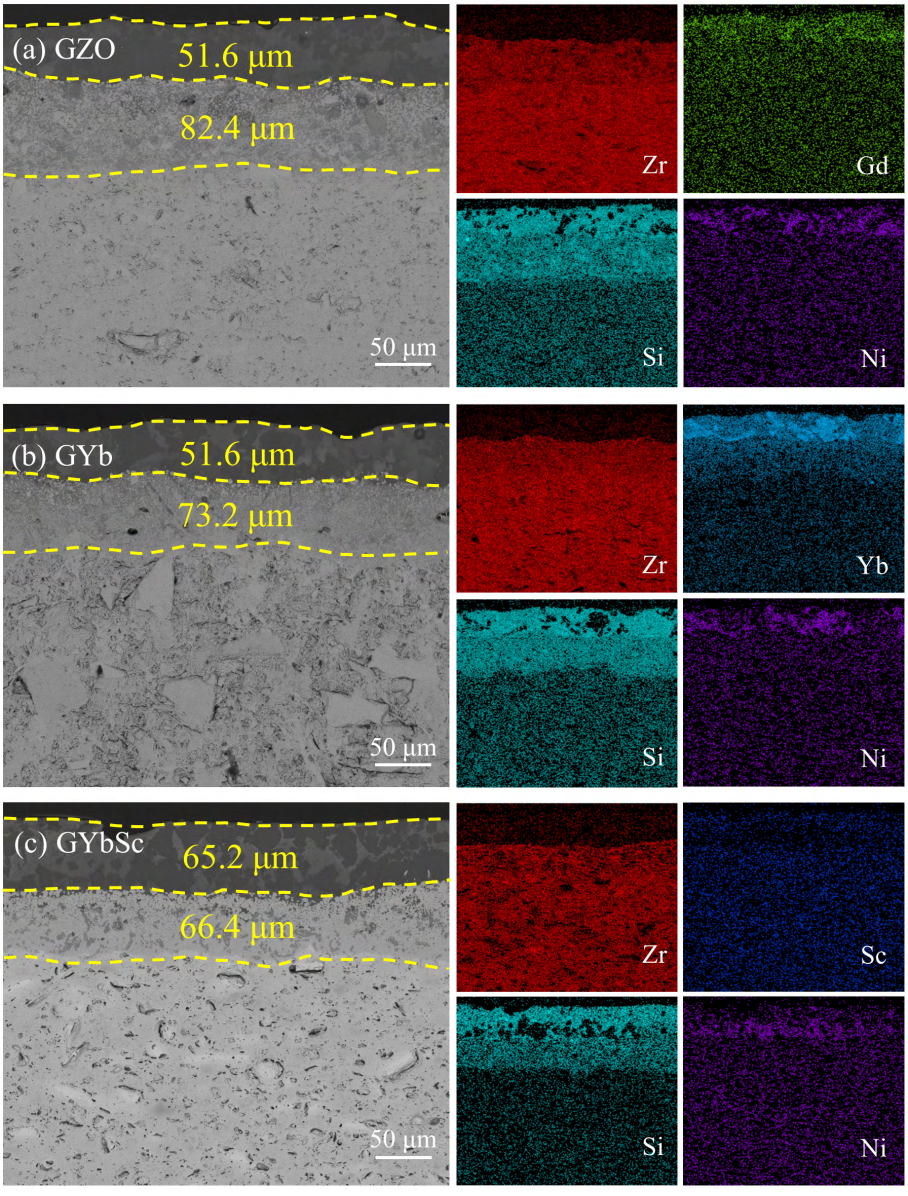

Fig. 10 Cross-sectional microstructure and corresponding EDS mappings of (a) GZO, (b) GYb, and (c) GYbSc following secondary coating of CMAS and heat treatment at 1250 °C for 10 min.

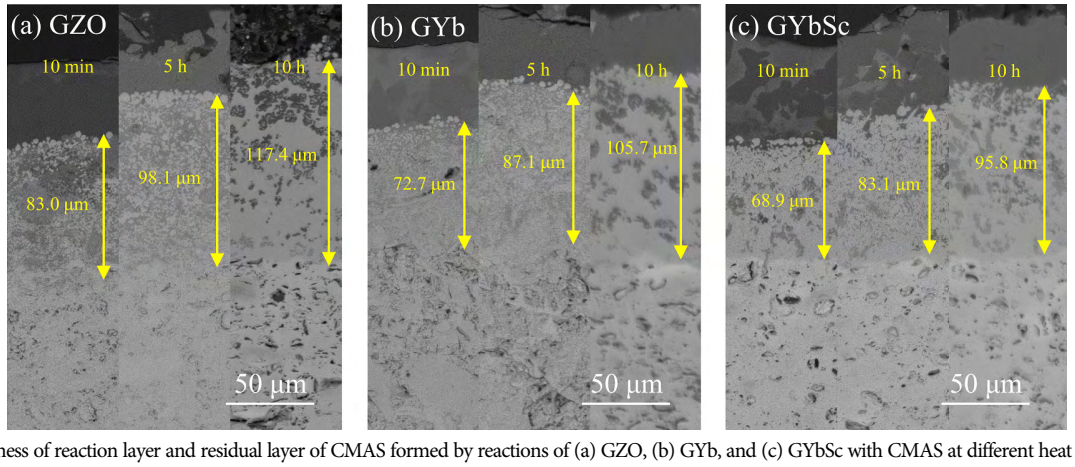

Fig. 11 Thickness of reaction layer and residual layer of CMAS formed by reactions of (a) GZO, (b) GYb, and (c) GYbSc with CMAS at different heat treatment time following secondary coating of CMAS.

lattice, forming a substitutional solid solution. With further introduction of Sc into Yb-doped GZO, Sc atoms occupy interstitial sites in the GZO lattice when their content is below 5.88 at%. The calculated mechanical and thermophysical properties show that among the GZO, Yb-doped GZO, and Yb–Sc codoped GZO systems, GYbSc exhibits the lowest thermal conductivity, the highest coefficient of thermal expansion, and a relatively high toughness, indicating its strong potential as a thermal barrier coating material.

(2) The experimental results show that 12.5 at% Yb substitutes for Gd in GZO, 11.76 at% Yb substitutes for Gd, and 5.88 at% Sc occupies interstitial sites in GZO, verifying the accuracy of the previous calculations. The lattice distortion caused by Yb substitution for Gd enhances phonon scattering, resulting in a lower thermal conductivity for GYb. The introduction of Sc into GYb intensifies lattice distortion, and interstitial doping can simultaneously reduce the oxygen vacancies in the crystal. Thus, GYbSc has a higher hardness, fracture toughness, and coefficient of thermal expansion, as well as a lower thermal conductivity, than GZO and GYb. The hardness and fracture toughness of GYbSc reach 12.76 GPa and 2.09 $MPa{\cdot}m^{1/2}$, respectively. GYbSc exhibits a coefficient of thermal expansion of 11.059×10^{-6} K^{-1} at 1300 °C, and its thermal diffusivity and thermal conductivity are 0.27 $mm^2{\cdot}s^{-1}$ and 0.935 $W{\cdot}m^{-1}{\cdot}K^{-1}$ at 1200 °C, respectively.

(3) During long-term corrosion, GYbSc exhibits superior resistance to CMAS corrosion compared with GZO and GYb. The reaction layer formed between GYbSc and CMAS is the thinnest, and a large amount of residual CMAS remains on the surface. The reactivity of Sc with CMAS is weak and does not lead to the formation of apatite phases. The relatively slow diffusion of Sc in molten CMAS helps enhance the interfacial stability of GYbSc, thereby endowing it with optimal CMAS corrosion resistance.

Acknowledgements

This research is sponsored by the Innovation Project (No. D9625BCD) and the National Natural Science Foundation of China (Nos. 52471087 and U2541255).

Availability of data and materials

The data that support the findings of this study are available from the corresponding author upon reasonable request.

Competing interests

The authors have no competing interests to declare that are relevant to the content of this article. The author Lei Guo is the Editorial Committee member of this journal.

Electronic Supplementary Material

Supplementary material is available in the online version of this article at https://doi.org/10.26599/JAC.2026.9221295.

References

[1] Darolia R. Thermal barrier coatings technology: Critical review, progress update, remaining challenges and prospects. *Int Mater Rev* 2013, **58**: 315–348.

[2] Sezavar A, Sajjadi SA. A review on the performance and lifetime improvement of thermal barrier coatings. *J Eur Ceram Soc* 2025, **45**: 117274.

[3] Wei ZY, Meng GH, Chen L, *et al.* Progress in ceramic materials and structure design toward advanced thermal barrier coatings. *J Adv Ceram* 2022, **11**: 985–1068.

[4] Kumar V, Balasubramanian K. Progress update on failure mechanisms of advanced thermal barrier coatings: A review. *Prog Org Coat* 2016, **90**: 54–82.

[5] Liu DR, Song WJ, He WT, *et al.* Modeling the viscosity and infiltration kinetics of silicate melt-thermal barrier coating systems based on deep-learning and experimental approach. *Acta Mater* 2025, **292**: 121081.

[6] Guo YQ, Luo Z, Song X, *et al.* Mitigating CMAS attack during thermal cycling via triple-scale micro/nano structured thermal barrier coatings. *J Mater Sci Technol* 2026, **251**: 180–192.

[7] Yin Q, Shen KH, Wang Y, *et al.* Research progress of rare earth zirconate thermal barrier coating ceramic materials. *Mater Today Commun* 2025, **42**: 111579.

[8] Shen ZY, Liu GX, Mu RD, *et al.* Effects of Er stabilization on thermal property and failure behavior of $Gd_2Zr_2O_7$ thermal barrier coatings. *Corros Sci* 2021, **185**: 109418.

[9] Lee KS, Jung KI, Heo YS, *et al.* Thermal and mechanical properties of sintered bodies and EB-PVD layers of Y_2O_3 added $Gd_2Zr_2O_7$ ceramics for thermal barrier coatings. *J Alloy Compd* 2010, **507**: 448–455.

[10] Yan ZH, Xie M, Li RY, *et al.* Reduced thermal conductivity of $Gd_2Zr_2O_7$ used in thermal barrier coatings due to Ti^{4+}–Ce^{4+} co-doping. *Ceram Int* 2025, **51**: 41723–41732.

[11] Liu B, Zhao JL, Liu YC, *et al.* Application of high-throughput first-principles calculations in ceramic innovation. *J Mater Sci Technol* 2021, **88**: 143–157.

[12] Liu YC, Chu KL, Zhou Y, *et al.* Discovery of orthorhombic perovskite oxides with low thermal conductivity by first-principles calculations. *J Adv Ceram* 2022, **11**: 1596–1603.

[13] Wong DF, Young K, Ng KYS. First-principles study of structure, initial lattice expansion, and pressure-composition-temperature hysteresis for substituted $LaNi_5$ and $TiMn_2$ alloys. *Model Simul Mater Sc* 2016, **24**: 085007.

[14] Winczewski S, Dziedzic J, Miruszewski T, *et al.* Properties of oxygen vacancy and hydrogen interstitial defects in strontium titanate: DFT+$U^{d,p}$ calculations. *J Phys Chem C* 2022, **126**: 18439–18465.

[15] Guo L, Guo HB, Peng H, *et al.* Thermophysical properties of Yb_2O_3 doped $Gd_2Zr_2O_7$ and thermal cycling durability of $(Gd_{0.9}Yb_{0.1})_2Zr_2O_7$/YSZ thermal barrier coatings. *J Eur Ceram Soc* 2014, **34**: 1255–1263.

[16] Zhen Z, Wang X, Shen Z, *et al.* Phase stability, thermo-physical property and thermal cycling durability of Yb_2O_3 doped $Gd_2Zr_2O_7$ novel thermal barrier coatings. *Ceram Int* 2022, **48**: 2585-2594.

[17] Guo WX. Study of the physical properties of Yb_2O_3-doped $Gd_2Zr_2O_7$ ceramics as a thermal barrier coating material. *Manuf Rev* 2025, **12**: 26.

[18] Guo L, Li BW, Cheng YX, *et al.* Composition optimization, high-temperature stability, and thermal cycling performance of Sc-doped $Gd_2Zr_2O_7$ thermal barrier coatings: Theoretical and experimental studies. *J Adv Ceram* 2022, **11**: 454–469.

[19] Li BW, Sun JY, Guo L. CMAS corrosion behavior of Sc doped $Gd_2Zr_2O_7$/YSZ thermal barrier coatings and their corrosion resistance mechanisms. *Corros Sci* 2021, **193**: 109899.

[20] Kresse G, Furthmüller J. Efficient iterative schemes for *ab initio* total-energy calculations using a plane-wave basis set. *Phys Rev B* 1996, **54**: 11169–11186.

[21] Hohenberg P, Kohn W. Inhomogeneous electron gas. *Phys Rev* 1964, **136**: B864–B871.

[22] Cheng CY, Chen L, Luo JH, *et al.* Initial corrosion mechanism of $Hf_6Ta_2O_{17}$ ceramic for TBCs against CMAS infiltration: Experiment and first-principle simulation. *Corros Sci* 2023, **225**: 111626.

[23] Yang L, Wang PY, Zhang CG, *et al.* Composition-dependent intrinsic defect structures in pyroclore $RE_2B_2O_7$ (RE = La, Nd, Gd; B = Sn, Hf, Zr). *J Am Ceram Soc* 2020, **103**: 645–655.

[24] Wang JH, Yip S, Phillpot SR, *et al.* Crystal instabilities at finite strain. *Phys Rev Lett* 1993, **71**: 4182–4185.

[25] Haines J, Léger JM, Bocquillon G. Synthesis and design of superhard materials. *Annu Rev Mater Res* 2001, **31**: 1–23.

[26] Wu ZJ, Zhao EJ, Xiang HP, *et al.* Crystal structures and elastic properties of superhard IrN_2 and IrN_3 from first principles. *Phys Rev B* 2007, **76**: 054115.
[27] Hill R. The elastic behaviour of a crystalline aggregate. *Proc Phys Soc A* 1952, **65**: 349–354.
[28] Luo F, Li BS, Guo ZC, *et al. Ab initio* calculation of mechanical and thermodynamic properties of $Gd_2Zr_2O_7$ pyrochlore. *Mater Chem Phys* 2020, 243: 122565.
[29] Green DJ. *An Introduction to the Mechanical Properties of Ceramics*. Cambridge (UK): Cambridge University Press, 1998.
[30] Kittel C. *Introduction to Solid State Physics*. New York (USA): Wiley, 1997.
[31] Zhao FA, Xiao HY, Liu ZJ, *et al.* A DFT study of mechanical properties, thermal conductivity and electronic structures of Th-doped $Gd_2Zr_2O_7$. *Acta Mater* 2016, **121**: 299–309.
[32] Wang XQ, Bai X, Xiao W, *et al.* Calculation of thermal expansion coefficient of rare earth zirconate system at high temperature by first principles. *Materials* 2022, **15**: 2264.
[33] Clarke DR. Materials selection guidelines for low thermal conductivity thermal barrier coatings. *Surf Coat Tech* 2003, **163**: 67–74.
[34] Clarke DR, Levi CG. Materials design for the next generation thermal barrier coatings. *Annu Rev Mater Res* 2003, **33**: 383–417.
[35] Cahill DG, Watson SK, Pohl RO. Lower limit to the thermal conductivity of disordered crystals. *Phys Rev B* 1992, **46**: 6131–6140.
[36] Guo L, Li G, Gan ZL. Effects of surface roughness on CMAS corrosion behavior for thermal barrier coating applications. *J Adv Ceram* 2021, **10**: 472–481.
[37] Evans AG, Charles EA. Fracture toughness determinations by indentation. *J Am Ceram Soc* 1976, **59**: 371–372.
[38] Thomson JB, Armstrong AR, Bruce PG. An interstitial pyrochlore formed by chemical intercalation of oxygen. *Chem Commun* 1996, **10**: 1165-1166.
[39] Shannon RD. Revised effective ionic radii and systematic studies of interatomic distances in halides and chalcogenides. *Acta Crystallogr A* 1976, **32**: 751–767.
[40] Wan CL, Pan W, Xu Q, *et al.* Effect of point defects on the thermal transport properties of $(La_xGd_{1-x})_2Zr_2O_7$: Experiment and theoretical model. *Phys Rev B* 2006, **74**: 144109.
[41] Liu DR, He WT, Wei LL, *et al.* Enhanced radiative cooling of columnar thermal barrier coatings at ultrahigh temperatures and mechanisms underneath. *J Mater Sci Technol* 2025, **239**: 81–92.
[42] Thompson JA, Clyne TW. The effect of heat treatment on the stiffness of zirconia top coats in plasma-sprayed TBCs. *Acta Mater* 2001, **49**: 1565–1575.
[43] Huang B, Ma ZS. Structural, elastic, thermal and mechanical properties of $LnTa_2O_6$ (Ln = Ce–Tb) ceramics from first-principles calculations. *Mater Today Commun* 2022, **31**: 103251.
[44] Evans AG, Mumm DR, Hutchinson JW, *et al.* Mechanisms controlling the durability of thermal barrier coatings. *Prog Mater Sci* 2001, **46**: 505–553.
[45] Pugh SF. XCII. Relations between the elastic moduli and the plastic properties of polycrystalline pure metals. *Lond Edinb Dublin Philos Mag J Sci* 1954, **45**: 823–843.
[46] Frantsevich IN, Voronov FF, Bokuta SA. *Elastic Constants and Elastic Moduli of Metals and Insulators Handbook*. Kiev (Ukraine): Naukova Dumka, 1982.
[47] Bouhadda Y, Djellab S, Bououdina M, *et al.* Structural and elastic properties of $LiBH_4$ for hydrogen storage applications. *J Alloy Compd* 2012, **534**: 20–24.
[48] Zhao M, Ren XR, Pan W. Mechanical and thermal properties of simultaneously substituted pyrochlore compounds $(Ca_2Nb_2O_7)_x(Gd_2Zr_2O_7)_{1-x}$. *J Eur Ceram Soc* 2015, **35**: 1055–1061.
[49] Zhao M, Pan W, Wan CL, *et al.* Defect engineering in development of low thermal conductivity materials: A review. *J Eur Ceram Soc* 2017, **37**: 1–13.
[50] Yeh JW. Recent progress in high-entropy alloys. *Eur J Control* 2006, **31**: 633–648.
[51] Schmitt MP, Stokes JL, Gorin BL, *et al.* Effect of Gd content on mechanical properties and erosion durability of sub-stoichiometric $Gd_2Zr_2O_7$. *Surf Coat Tech* 2017, **313**: 177–183.
[52] Mori M, Hiei Y, Sammes NM, *et al.* Thermal-expansion behaviors and mechanisms for Ca- or Sr-doped lanthanum manganite perovskites under oxidizing atmospheres. *J Electrochem Soc* 2000, **147**: 1295.
[53] Wang J, Zeng YP, Chong XY, *et al.* Superior thermal and oxygen barrier properties of high-entropy ferroelastic rare earth tantalate $(8RE_{1/8})TaO_4$. *J Adv Ceram* 2024, **13**: 2051–2067.
[54] Li MZ, Guo L, Ye FX. Phase structure and thermal conductivities of Er_2O_3 stabilized ZrO_2 toughened $Gd_2Zr_2O_7$ ceramics for thermal barrier coatings. *Ceram Int* 2016, **42**: 16584–16588.
[55] Tye RP. *Thermal Conductivity*. New York (USA): Academic Press, 1969.
[56] Berman R. *Thermal Conduction in Solids*. Oxford (UK): Clarendon Press, 1976.
[57] Ratsifaritana CA, Klemens PG. Scattering of phonons by vacancies. *Int J Thermophys* 1987, **8**: 737–750.
[58] Pan W, Liu GH, Wang XL, *et al.* Review of the development of thermal barrier coating materials and technologies. *Therm Spray Techn* 2025, 17: 1–17. (in Chinese)
[59] Duffy JA. Acid–base reactions of transition metal oxides in the solid state. *J Am Ceram Soc* 1997, **80**: 1416–1420.
[60] Krause AR, Senturk BS, Garces HF, *et al.* $2ZrO_2{\cdot}Y_2O_3$Thermal barrier coatings resistant to degradation by molten CMAS: Part I, optical basicity considerations and processing. *J Am Ceram Soc* 2014, **97**: 3943–3949.
[61] Dimitrov V, Komatsu T. Classification of simple oxides: A polarizability approach. *J Solid State Chem* 2002, **163**: 100–112.